GEOLOGICAL SURVEY OF CANADA
OPEN FILE 7457

SEDEX Mineralisation, Macmillan Pass (Yukon): Petrography, Mineralogy and Bulk Geochemistry of the Tom and Nidd Deposits

J.M. Magnall, S.A. Gleeson, and S. Paradis

2014

Natural Resources Canada | Ressources naturelles Canada

Canada

GEOLOGICAL SURVEY OF CANADA
OPEN FILE 7457

SEDEX Mineralisation, Macmillan Pass (Yukon): Petrography, Mineralogy and Bulk Geochemistry of the Tom and Nidd Deposits

J.M. Magnall[1], S.A. Gleeson[1], and S. Paradis[2]

[1] Department of Earth and Atmospheric Sciences, University of Alberta, Edmonton, AB T6G 2E3
[2] Geological Survey of Canada (Sidney), 9860 West Saanich Road, Sidney, BC V8L 4B2

2014

doi:10.4095/293105

This publication is available for free download through GEOSCAN (http://geoscan.ess.nrcan.gc.ca/).

Recommended citation
Magnall, J.M., Gleeson, S.A., and Paradis, S., 2014. SEDEX Mineralisation, MacMillan Pass (Yukon): Petrography, Mineralogy and Bulk Geochemistry of the Tom and Nidd Deposits; Geological Survey of Canada, Open File 7457. doi:10.4095/293105

Publications in this series have not been edited; they are released as submitted by the author.

INTRODUCTION 5

REGIONAL GEOLOGY 5

LOCAL GEOLOGY 6

ANALYTICAL TECHNIQUES AND DATA COLLECTION 8
- Petrography 8
- Electron Probe Micro Analyser (EPMA) 8
- Major, Minor and Trace Element Geochemistry 8

RESULTS 9
- Petrography and Mineralogy 9
- Description and Paragenesis – Vent Complex at the Tom and Nidd Deposits 10
- Description and Paragenesis – Stratabound Mineralisation at the Tom Deposit 11
- Alteration 12
- Deformation 13
- Bulk Geochemistry 13

DISCUSSION 14
- Mineral Paragenesis 14
- Depositional Environment of the Host rock 14
- Textural Interpretation: evidence for syn-sedimentary mineralisation? 15
- Bulk Geochemistry 16

CONCLUSIONS 17

REFERENCES 18

ABSTRACT

Sedimentary exhalative (SEDEX) deposits formed in the Selwyn Basin coeval with 3 magmatic episodes in the Cambrian, Silurian and Late Devonian. At Macmillan Pass, the Tom, Jason and Nidd deposits are hosted by Late Devonian strata and have well preserved vent complexes beneath overlying stratabound sulphide and sulphate facies.

Drill core has been sampled from the vent complexes at Nidd and Tom. Detailed petrography (reflected and transmitted light, cathodoluminescence, back-scatter electron imaging) has developed a paragenesis and, at Tom, critically assessed textural relationships between the vent facies and the overlying stratabound sulphide and sulphate facies. The mineral chemistry of major phases has been determined from quantitative electron microprobe analyses in the vent and stratabound ore from Tom. The geochemical signatures of the hydrothermal vents (Tom, Nidd) are comprehensively characterized through bulk rock geochemical analysis of vent facies material for major, minor and rare earth elements.

Detailed petrography has highlighted subtle feeder veins that preferentially replaced laminations leading to the formation of pseudo-bedded sulphide-rich layers in the grey facies rocks at Tom. This provides an important link between the vent and the overlying stratabound facies. Within the vent, main stage sulphide minerals succeeded destructive carbonate alteration, and were overprinted by pulses of sulphide minerals coeval with, and replacing, siderite, Ba-carbonate and barite. Aside from the ore components (Pb, Zn and Ba), vent facies samples are enriched above upper crustal values in Au, Ag, As, Cd, Cu, Ge, In, Mo, Sb, Sn and Ta. Notably, Au in two samples from Tom exceeds 100 ppb. Rare-earth element profiles broadly track the composition of un-mineralised shale in the area but have a positive Eu anomaly, likely attributable to the presence of Ba feldspar in the samples. This highlights the potential importance of the compositions of underlying strata in controlling the geochemistry of the hydrothermal fluids.

INTRODUCTION

The Tom, Nidd and Jason Zn-Pb SEDEX deposits are located at Macmillan Pass (map sheet 105 O/1), Yukon Territory, adjacent to the NWT border and approximately 390 km NE of Whitehorse (63° 11' N, 30° 21' W) (**Figure 1**). They are hosted within late Devonian Selwyn Basin strata, specifically, a package of siliceous shales, mudstones and siltstones, and coarser-grained siliciclastic rocks, formally defined as the Earn Group by Gordey et al. (1982). The deposits all contain a zone of hydrothermal upflow, i.e. a hydrothermal vent, which forms a key genetic feature beneath the stratabound ore of SEDEX deposits (Goodfellow *et al.,* 1993; Goodfellow and Lydon, 2007). Although SEDEX deposits are reported elsewhere in the geological record it is rare to find vent complexes that are as well preserved as those at MacMillan Pass. These deposits therefore offer the opportunity to fully characterize the mineralogical relationships and bulk geochemistry of a vent complex. This report presents the results of detailed petrography, mineralogy and bulk geochemistry produced on vent complex samples from two of the three deposits located at MacMillan Pass (Tom and Nidd), in conjunction with petrography and mineralogy of overlying stratabound ore from Tom.

REGIONAL GEOLOGY

The Selwyn Basin was originally defined by Gabrielse (1967) as a thick, westward thickening wedge of strata of Precambrian to Middle Devonian age, deposited along the western margin of ancestral North America. The onset of basinal sedimentation was instigated by rifting associated with the continental breakup of Rhodinia (~760 Ma), leading to passive margin sedimentation and forming what has traditionally been referred to as the Cordilleran *miogeocline* (Eisbacher, 1985; Gordey and Anderson, 1993; Goodfellow *et al.,* 1995; Dickinson, 2004). The basin is now defined in terms of deep-water off-shelf sedimentation of late Precambrian to Middle Devonian age, with rift clastics forming basal and overlying deposits from the late Precambrian and Late Devonian, respectively (Gordey and Anderson, 1993). Rocks of the Windermere Supergroup form the basement and are the oldest exposed rocks in the Selwyn Basin, comprising a 4-6km sequence of Hadrynian-Cambrian clastic sedimentary rocks deposited following the erosion of the crystalline basement during continental breakup (Eisbacher, 1985).

During the late Devonian-Mississippian, thick accumulations of coarse clastic sediments were deposited over the basinal strata of the Selwyn Basin. Regionally, this marked a change from an Atlantic-style passive margin to a West Pacific style convergent margin, as the western margin of

ancestral North America collided with an island arc and extensional tectonics were re-activated as rifting was generated by slab roll back in a distant back-arc setting (Nelson *et al.*, 2002; Lund *et al.*, 2008). This tectonic setting formed the backdrop to an important period of volcanogenic massive sulphide (VMS) metallogenesis within allochthonous pericratonic terranes in the immediate back-arc and intra-arc settings; more distant back-arc settings formed the proposed environment of SEDEX mineralisation (Nelson and Colpron, 2007; Goodfellow, 2007).

Three episodes of magmatic activity have been identified during passive margin sedimentation, with mafic volcanic flows, dykes and tuffs observed in Early Cambrian, Middle Ordovician, and Middle to Late Devonian strata (Goodfellow, 2007). The observation of alkalic and ultrapotassic volcanic rocks associated with syn-rift clastic rocks during the lower to middle Paleozoic has been used as evidence for widespread extensional tectonics; the incompatible element chemistry of these units suggests an origin similar to that observed in alkaline basalts formed in continental rifts (Goodfellow *et al.*, 1995). Intrusive rocks of mid-Cretaceous to Tertiary (124-62 Ma) age form the final component of Selwyn Basin regional geology. They were emplaced into the deformed continental strata produced during Mesozoic island arc accretion, and they provide an important setting for intrusion related deposits (Hart *et al.*, 2004; Thiessen *et al.*, 2011).

As a result of deformation related to Mesozoic island arc accretion, the miogeoclinal strata have been incorporated into the northern Cordillera fold and thrust belt. Basinal strata form the *inner belt*, characterised by regional-scale folds and thrusts and accompanied by slaty cleavage and intense tight to isoclinal folding; platformal carbonates form the *outer belt* and represent the eastern most extent of deformation (Gordey *et al.*, 2010). The final age of deformation is late Early Cretaceous, as determined by crosscutting of strata by mid-Cretaceous plutonic rocks (Gordey *et al.*, 2010).

LOCAL GEOLOGY

The Zn-Pb SEDEX deposits of Tom, Nidd and Jason are hosted in the Earn Group, which contains the Portrait Lake Formation (lower Earn Group) and Prevost Formation (upper Earn Group) (see **Figure 2**). The main phase of Zn-Pb stratabound mineralisation was localized within the Portrait Lake Formation, specifically within the Macmillan Pass Member (Abbott and Turner, 1990). This member contains pebble conglomerate, diamictite interbedded with sand and shale, and silt laminated mudstone (Abbott and Turner, 1990; Magnall and Gleeson, 2012a). Variability in bed thickness of the coarse clastics in the local area of Macmillan Pass has been interpreted to represent the existence of a

number of basin-bounding faults and sedimentation in a syn-tectonic environment (Abbott and Turner, 1990).

The host rock to the Tom (West Zone) and Jason deposits has been dated as mid-Frasnian by conodont biostratigraphy (Irwin and Orchard, 1991). Mineralisation at Macmillan Pass has traditionally been considered syn-sedimentary, and so this biostratigraphic marker has been used to constrain the timing of hydrothermal mineralisation (Goodfellow *et al.*, 1993; Goodfellow and Lydon, 2007). Macmillan Pass also hosts stratabound barite deposits within the same stratigraphic horizon as base metal deposits, potentially representing the distal expression of the hydrothermal activity that produced Tom and Jason (Goodfellow and Lydon, 2007; Fernandes, 2011). 15 km west of Jason, the epigenetic Pb-Zn sulphide minerals at Boundary Creek (Nidd) are similar to those at Tom and Jason, and are also hosted by the Macmillan Pass Member (Turner and Rhodes, 1990; Magnall and Gleeson, 2012b). As no stratabound sulphide minerals are observed at Nidd, it is possible that this occurrence represents either a failed feeder zone or that the overlying stratabound facies was not preserved.

Tom, Jason and Nidd are located within the central block of the Macmillan Fold Belt (MFB), formed during Mesozoic deformation and characterized by west-trending folds that contrast with the more northwest regional trend (Abbott, 1982). Structures are clearly Mesozoic in age, but the differences in style between the blocks of the MFB indicate that deformation may be influenced by pre-existing Devonian structures (Abbott, 1982; Abbott and Turner, 1990).

ANALYTICAL TECHNIQUES AND DATA COLLECTION

Petrography

Samples were collected from drill core storage (MacMillan Pass, YT) at Nidd (2010 field season) and Tom (2012 field season). Samples of coarse vent facies (Nidd, Tom) and stratabound facies (Tom) were targeted along with under- and overlying strata. Hand samples were described and ~100 thin sections were made for detailed optical microscopy under reflected and transmitted light. A desktop cold cathode-tube cathodoluminscence microscope (University of Alberta) was used to examine compositional and textural relationships between different generations of quartz at Nidd.

Electron Probe Micro Analyser (EPMA)

The JEOL 8900 (University of Alberta, Electron Microprobe Laboratory) was used for backscatter electron (BSE) imaging, wavelength dispersive spectroscopy (WDS) and electron dispersive spectroscopy (EDS). These techniques were used to examine compositional zoning, textural relationships and mineral chemistry (major elements). The electron beam was operated at an accelerating voltage of 15kV, a probe current of 15nA and a beam diameter of 5μm (barite, silicates). For barite, the standards used were apatite (P_2O_5), barite (BaO and SO_3), diopside (CaO and SiO_2), forsterite-93 (MgO), hematite (FeO), sanidine (K_2O) and strontianite (SrO). For the silicates, owing to high Ba concentrations, Ba-niobate was used for Ba, albite (Na_2O), microcline (K_2O), anorthite (SiO_2, CaO, Al_2O_3), fayalite (FeO), diospide (MgO) and willemite (MnO). For sulphides, the equipment was operated with a 20kV accelerating voltage, 20nA, and 5μm beam diameter. Standards used were galena (Pb), arsenopyrite (As), bismuth-metal (Bi), pyrite (Fe, S), silver-metal (Ag), antinomy-metal (Sb), copper-metal (Cu), tin-metal (Sn), tungsten-metal (W), sphalerite (Zn) and gold-metal (Au). Only those analyses producing totals ±2% of 100% have been reported and all results below a detection limit of 3σ have been disregarded. Detection limits are displayed in the results section.

Major, Minor and Trace Element Geochemistry

Vent samples from Nidd (n = 3) and Tom (n = 14) were analysed for major element oxides, minor and trace elements at Activation Laboratories, Ancaster (Ontario). Minor and trace elements were analysed via instrumental neutron activation analysis (INAA) and inductively coupled plasma mass spectrometry (ICP-MS). Major element oxides were analysed on bulk rock powders (prepared to minus 150 mesh) via lithium metaborate / tetraborate fusion-ICP.

In-lab standards traceable to certified standard reference materials (SRM's) and certified SRM's were used for quality control. Only data above detection limit of 3σ has been reported.

RESULTS

Petrography and Mineralogy

A summary paragenetic sequence for Tom is presented in **Figure 3** along with summary tables of EPMA data for the mineral chemistry of major constituents (**Tables 1, 2** and **3**). Detailed descriptions of the paragenetic stages of mineralisation for Tom and Nidd will follow. Past authors have used terminology that describes the mineral assemblages in terms of facies, with the stratabound portion of the deposit split into the *pink, grey* and *black facies* and the vent mineral assemblage referred to as the *vent facies* (Goodfellow and Lydon, 2007). This terminology will also be used here.

Sulphide minerals: In order of relative abundance the sulphide minerals observed in the vent and stratabound ore are as follows; pyrite, sphalerite, galena, chalcopyrite, pyrrhotite, arsenopyrite (with minor tetrahedrite and bournonite). A summary of the mineral chemistry of major phases is given in **Table 1**. The enrichments in Au are not recorded in any of the major sulphide phases whereas chalcopyrite, sphalerite and galena have higher Ag contents than those found in the bulk geochemistry results (>100ppm).

Carbonates: ankerite, siderite, calcite and barytocalcite were observed at different stages of the paragenesis. A summary of their mineral chemistry is given in **Table 2**. Both barytocalcite and ankerite contain notable concentrations of Sr (>2000ppm).

Silicates: within the stratabound ore, the barium feldspars celsian and hyalophane are observed, occurring at the top of mudstone beds, early in the paragenesis. A summary of their mineral chemistry is given in **Table 3** and results plotted on a feldspar ternary plot (**Figure 4**). The earliest phase, hyalophane, is volumetrically less significant than celsian. Notably, hyalophane analyses returned low cation totals (4.92). These results fall within the range recorded by Fernandes (2011) in Late Devonian baritic mudstones from Macmillan Pass. The end member Ba-feldspar, celsian, forms the majority of analyses with compositions that closely compare with Moro *et al.*, (2001).

Description and Paragenesis – Vent Complex at the Tom and Nidd Deposits

Tom: rocks of the vent facies are distinctively orange in colour, and are characterised by Fe-carbonate stockwork style veining (>1cm thick; **Figure 5A, B**). Clasts of host rock (mudstone) are locally discernible depending on the extent of overprinting by hydrothermal veining and alteration. The host-rock has similar characteristics to the mudstone found in the *Grey Facies* located above the vent, to be described in a subsequent section. Vent material is enriched in sulphides, with some samples consisting of >30% galena (± pyrite, ±sphalerite, ±pyrrhotite, ±chalcopyrite).

Stage 1 mineralisation at Tom is typified by a simple assemblage of pyrite + ankerite + quartz. Large (>> 500μm) pyrite euhedra form within interlocking crystals of anhedral ankerite (**Figure 6A**). This ankerite is the most volumetrically significant Fe-carbonate and it replaces the host rock. Large (<< 500μm) subhedral quartz crystals have undulose extinction and are intergrown with ankerite in textural equilibrium. Multiple generations of this assemblage have been observed, with small veinlets of ankerite and quartz found crosscutting each other.

Stage 2 at Tom was the main period of sulphide mineralisation. Pyrite (Py-IIa), the first phase to form, displays a distinctive, fine-grained colloform texture (**Figure 6B**). This generation of pyrite is postdated by a series of minerals that overprint and crosscut the Stage 1 assemblage in small veins. Volumetrically, pyrite and galena are dominant. Pyrite-IIa was recrystallized, cataclastically deformed and overprinted by a second stage of pyrite (Py-IIb) that forms large euhedral crystals. Galena ± pyrrhotite ± (tetrahedrite, bournonite) destructively replaced earlier Stage 1 and 2 minerals, corroding pyrite and ankerite (**Figure 6C and D**). Veinlets of Fe and Ba-rich carbonate (±siderite, ±barytocalcite, ±witherite), associated with chalcopyrite and galena, crosscut earlier paragenetic stages (**Figure 6E and F**).

Nidd: the vent at Nidd is much more discrete than at Tom. Hydrothermal veining and alteration is much less intense, and dark grey to black mudstone forms a greater proportion of the rock (**Figure 5C**). Veins are rusty-brown and rich in sphalerite and Fe-carbonate. They are locally banded and range between 5mm to 2-3cm in size, anastomosing around clasts of brecciated host rock.

Stage 1 ore and alteration minerals are much less extensive at Nidd than at Tom. Strata above and below the vent display some characteristics of Stage 1 fluid flow, with widespread Fe-carbonate and pyrite cementing conglomerate and sandstone beds. Vent samples do not display these features.

Stage 2 minerals at Nidd fill discrete veins within dark grey to black mudstone. Pyrite, quartz and barite typically formed first along vein margins (**Figure 7**), with the latter occurring as fibrous to radiaxial crystals, (200-300μm) that form interlocking textures with similarly sized crustiform and

comb quartz (classified according to Dong et al., 1995). Pyrite occurs as fractured anhedral to euhedral aggregates along the margin of the host rock. In a few places euhedral siderite rhombs formed after barite and quartz. These gangue minerals were invaded by fine-grained, rusty red – brown sphalerite (Sp-IIa) hosting abundant chalcopyrite and rarer inclusions of galena and tetrahedrite; within thicker veins rusty red – brown sphalerite grades into red sphalerite (Sp-IIb), in turn replaced by a clear to light tan coloured generation (Sp-IIc). At the center of veins euhedral siderite represents the final phase of vein mineralisation.

Description and Paragenesis – Stratabound Mineralisation at the Tom Deposit

Host rock: the dominant mineral in the mudstone is SiO_2, observed in thin section as microcrystalline quartz, set in a dark clay-rich matrix with sparse detrital quartz silt-size grains and minor rutile. Thicker mudstone beds do not display fissility, and so overall, the host rock is best described as a siliceous, calcareous mudstone. Locally, mudstone beds are homogenous and dominated by very fine-grained SiO_2 (cryptocrystalline quartz) and, therefore, are best classified as chert. Texturally, the mudstone displays some notable features. Wavy to lenticular laminations form ellipsoidal lenses (~500μm in length) of fine quartz silt (~5μm grain size) encased in a dark matrix of clay and organic material (**Figure 8A**) (e.g., O'Brien and Slatt, 1990). Laminations in places fine upward to homogenous, clay-rich mudstone; in other places the intercalated silt and mudstone laminae have sharper contacts. Common microcrystalline quartz-carbonate nodules (<100μm) are circular (**Figure 8B**), possibly representing recrystallized radiolarians.

Stratabound Mineralisation: This mudstone is host to the stratabound facies that overlies the vent complex. It is finely interlaminated with barite and sulphide minerals. It is locally calcareous, as indicated by effervescence with 10% HCl. Individual mudstone beds and laminations are generally thin (<3mm), planar, and dark grey to black. Barite, identified by softness and lack of effervescence, forms thin (1-2mm), fine-grained, white-grey coloured layers. Sphalerite is the primary sulphide present, forming thin (1-2mm), fine-grained, beige-pink coloured layers. Contacts between barite, sphalerite and mudstone layers are diffuse. Galena, identified by its grey, metallic lustre, forms more sharply defined layers. Pyrite is ubiquitous as euhedral crystals (>500μm) densely disseminated along certain laminae and sparser, finer grained disseminations within some mudstone beds. Where mudstone and barite form a greater proportion of the rock it is characteristically grey-black in colour (grey facies) whereas increasing sphalerite content produces samples with a more distinctive pink colour (pink facies).

Stage 1: the first stage of mineralisation in the stratabound ore involves the formation of a mineral assemblage of pyrite (Py-I), Ba-feldspars (celsian and hyalophane), and quartz. An early generation of barite (Ba-I) has also been included in this assemblage (see paragenesis), however it is volumetrically minor. Ba-I forms interlocking, subhedral, tabular crystals (~50μm) that occupy thin (<500μm) microcrystalline laminations within mudstone beds (**Figure 8C** and **D**). Pyrite-I has 3 distinct forms (a, b, c) that are not temporally distinguishable between each other but are all early. These include framboids (<20-30μm; Py-Ia), small euhedral crystals (~50μm; Py-Ib) and pyritized radiolarian tests (>100μm; Py-Ic). Barium-feldspars occur locally along the upper surface of well-preserved mudstone beds (**Figure 8E** and **F)**. EPMA indicates there to be two types present; celsian ($BaAl_2Si_2O_8$) forms large (500-100μm), euhedral, monoclinic crystals, and hyalophane ($(K,Ba)[Al(Si,Al)Si_2O_8]$) occurs as smaller (<200μm) more irregular, subhedral crystals.

Stage 2: hydrothermal veining and replacement typify the second stage of mineralisation in the stratabound ore. Pyrite (Py-II) is the earliest mineral to form, as large (>100μm), euhedral crystals that overprint and recrystallize earlier pyrite (Py-1a, b, c). A 2nd generation of barite (Ba-II) forms the majority of the barite in the stratabound ore as larger (>50μm), well-defined, equant, euhedral crystals that often occur in veins that cut mudstone laminae. Ba-II is clearly seen to overprint earlier formed textures and Ba-feldspars (indicated by etching of the crystal edges, e.g. **Figure 8E**). However Ba-II can also occur along stratal horizons and it is possible that this represents the recrystallization of Stage 1 Ba-I laminations. Notably, this generation of barite appears to overlap with Py-II, with some evidence for textural equilibrium between the two minerals.

Irregular veins of sulphide-bearing carbonates (calcite, barytocalcite, witherite) and quartz brecciate the mudstone beds and permeate along stratal horizons to produce irregular sulphide-rich stratabound layers (**Figure 9**). These layers overprint and replace the host-rock. With increasing distance from the vein source, sulphide layers become much less concentrated and more diffuse, forming minor interstitial blebs within the host rock (**Figure 9D**; **Figure 8D** may also be representative of a distal sulphide mineralisation). Individual blebs of sphalerite tend to be <30μm, sugary, fine-grained and light brown. Galena is found as inclusions within sphalerite-rich layers, and also as irregular blebs within the host rock.

Alteration

Samples from the vent complex and overlying stratabound ore are mostly affected by widespread carbonate alteration. In the vent, Stage 1 mineralisation is characterised by a destructive phase of

carbonate alteration (ankerite) that aggressively replaces the host rock. This is present both as hydrothermal veining, and also as fine-grained, patchy replacement textures to pre-existing host-rock. This latter alteration style is dominant within the overlying stratabound ore, and notably there is evidence of preferential fluid flow along stratal permeability.

Deformation

Evidence of two kinds of deformation is present within the samples from Nidd and Tom. In the stratabound ore at Tom, ductile deformation is evidenced in a variety of forms where layers of sulphide minerals and barite, and interbeds of mudstone display many features seemingly characteristic of soft-sediment deformation (SSD). These include irregular slump-style folding, convolute laminations and fluidization structures (**Figure 10**).

Also within the stratabound ore, late brittle deformation is represented by small-scale fracture sets between thicker beds, fine quartz-carbonate microveinlets (<50μm), and thicker, irregular, more distinct sulphide-bearing veins (**Figure 9**). Beneath the stratabound ore, the stockwork veining of the vent complex represents very distinctive brittle deformation. Multiple phases of deformation are evidenced by crosscutting veins, and on the micro-scale Stage 1 pyrite displays spectacular cataclastic deformation.

Bulk Geochemistry

The results of the bulk rock analysis for major, minor and trace elements of samples from Tom (n=14) and Nidd (n=3) are presented in Table 4. Low totals can be attributed to ore-grade concentrations (10-30 wt. %) of Pb and Zn that were too high to be determined by the analytical technique.

The North American Shale Composite (NASC; Gromet *et al.*, 1984) is used as a framework against which to compare the major element composition of vent samples from Tom and Nidd. **Figure 11** indicates vent samples from Tom display consistent enrichments in Fe_2O_3 and MnO, with MgO and CaO less consistent; samples are depleted relative to NASC in SiO_2, Al_2O_3, Na_2O, K_2O and P_2O_5. Nidd is broadly similar; however there is a small enrichment in Fe_2O_3 and a large depletion in CaO and MgO, whilst K_2O, TiO_2 and P_2O_5 more closely reflect the composition of the NASC.

When primary ore forming components (Pb, Zn, and Ba) are discounted, vent facies samples display enrichments in Au, Ag, As, Cd, Cu, Ge, In, Mo, Sb, Sn and Ta when compared to the composition of

the upper continental crust (McLennan, 2001; determined as an average of a compilation of clastic strata). Furthermore, two vent facies samples from Tom display notable enrichments in Au (>100ppb).

Figure 12 displays the rare earth elements (REE) profile of samples from Tom and Nidd, normalized with reference to the composition of a C1-carbonaceous chondrite (McDonough and Sun, 1995) and compared to the NASC (Gromet *et al.,* 1984; Taylor and McLennan, 1985) and the composition of a Late Devonian un-mineralised shale from the Selwyn Basin (Fernandes, 2011). The vent facies samples broadly track the NASC and un-mineralised Selwyn Basin shale apart from a positive Eu anomaly.

DISCUSSION

Mineral Paragenesis

In the previous fluid inclusion study at Tom (Ansdell *et al.,* 1989), analysis focused largely on samples from Stage 1 of the paragenesis (ankerite, quartz; this study), before the main stage of sulphide mineralisation. Ansdell *et al.,* (1989) recorded wide ranges in fluid salinity and temperature (2-18 wt.% equiv., 157-335°C). From the paragenesis interpreted in this study, it is apparent that their results record the analysis of the hydrothermal fluids responsible for Stage 1 fluid-flow. The value and reliability of these results for providing information on the ore-forming fluid is therefore questionable for multiple reasons. Stage 2 fluid flow may have formed secondary fluid inclusions within Stage 1 phases. In addition, hydrothermal fracturing during Stage 2 fluid flow may have deformed Stage 1 mineral phases, resulting in unreliable homogenization temperatures. Ultimately, Stage 1 mineral phases are not associated with sulphide minerals (Stage 2) therefore it is difficult to draw any reliable conclusions on the composition of the ore-forming fluid.

Depositional Environment of the Host rock

Sharp erosive contacts between individual laminations in mudstone beds indicate periodic reworking of the seafloor (Macquaker et al., 2010). At a smaller scale, the preservation of lenticular laminations suggests there was erosion and re-deposition of water-rich mud clasts (Schieber et al., 2010; Schieber, 2011). Evidence for high-energy conditions is further supported by the presence of heavy minerals such as rutile, which has been used as a proxy for energetic regimes typical of coastal environments (Dellwig et al., 2000). These features are observed within the mudstone interlaminations of the stratabound facies, indicating that host rock to the stratabound ore was unlikely deposited as pelagic

fallout in a low-energy sedimentary environment. This is supported by the observation of coarse clastics within the Macmillan Pass Member (Abbott and Turner, 1990). Sandstone, pebble conglomerate and diamictite all occur directly beneath the vent (Nidd, Tom) and stratabound facies (Tom) (Magnall and Gleeson, 2012a; Magnall and Gleeson, 2012b). If deposition of the coarse clastics was syn-tectonic, the same tectonism is likely responsible for driving hydrothermal fluid flow. Coarse clastics therefore form potential vectors to mineralisation.

Textural Interpretation: evidence for syn-sedimentary mineralisation?

The traditional model for SEDEX mineralisation at Macmillan Pass involves the syn-sedimentary precipitation of sulphides and barite above the sediment water interface (SWI) (Goodfellow and Lydon, 2007). At the hand sample scale, laminations between stratabound ore and mudstone do give the appearance of a sedimentary fabric. However, when evaluating these rocks, it is necessary to consider textures on the micro-scale. Furthermore, the effect of diagenesis and tectonic deformation processes should be evaluated, as they have the potential to remobilize phases and overprint primary textures, particularly for minerals such as galena. For this reason, only textures in well-preserved samples without evidence of major deformation have been assessed (e.g. **Figure 9**). It is with careful consideration of these factors that an attempt is made to evaluate the evidence for syn-sedimentary sulphide and barite mineral deposition within the stratabound ore at Tom.

Evidence for a primary, sedimentary component (precipitation above SWI) of barite preserved in the stratabound ore is limited. Microcrystalline barite laminations (Ba-I) are volumetrically minor, and their size (>50μm) and morphology (flat, tabular) is more in line with diagenetic barite sampled from modern day environments (Paytan *et al.*, 2002). The overwhelming majority of barite (Ba-II) occurs within Stage 2. In places the barite within Ba-I laminations appear to increase in crystal size (>>50μm), becoming more typical of Ba-II observed in veins elsewhere. This could represent remobilization of Ba-I below the SWI during diagenesis, and is supported by associated barite veinlets that crosscut mudstone lamina (**Figure 8C**). Furthermore, barite appears to form corrosive contacts with mudstone lamina, most clearly observed in reflected light and possibly representative of patchy replacement (**Figure 8D**).

It has been suggested that a fluctuating chemocline within the sediment can produce Ba remobilization and concentration along diagenetic fronts (Hendy, 2010; Henkel et al., 2012). This could explain the formation of secondary barite (Ba-II) from the remobilization of more microcrystalline, laminated barite (Ba-I) in the stratabound ore at Tom. Importantly, the formation of secondary barite would

require sulphate to be present in pore waters below the SWI during diagenesis. In addition, analysis of diagenetic barite would not provide a reliable record of the S and O isotope composition of seawater (Paytan *et al.*, 2004; Griffith and Paytan, 2012).

In contrast to barite there was no sulphide precipitation during Stage 1. All sulphide mineral paragenesis is placed within Stage 2, independent of barite. Although fine-grained interstitial sulphides (predominantly sphalerite) are localized along sedimentary laminae, these textures can be genetically linked to veining that post-dates sedimentation (**Figure 9**). These interstitial sulphides appear to form corrosive textures within and between mudstone laminations, interpreted to be horizons of preferential replacement. Considered together, barite and sulphide mineralisation could have been produced by a fluctuating chemocline within the strata that promoted the preferential precipitation of either sulphides or barite, depending on the redox state of pore fluids. This would remove the requirement for euxinic conditions above the SWI (Goodfellow and Lydon, 2007).

The occurrence of Ba-feldspars along the upper surface of well preserved mudstone beds is interesting. Hyalophane appears to have formed first, followed by celsian, and both phases are respectively overprinted, brecciated and veined by subsequent barite, quartz and base-metal sulphides. These mineralogical relationships suggest that Ba-feldspars formed during early diagenesis. A possible interpretation is that they formed in association with organic-rich, microbially stabilized horizons that developed during hiatuses in sedimentation; the influx of Ba-rich, hydrothermal fluid and interaction with degrading organic matter could have produced the conditions required for Ba-feldpsar crystallization (e.g. Orberger et al., 2005). It is notable, therefore, that the cation totals for the earliest formed Ba-feldspar, hyalophane, is low (4.92; Table 2). This could be a result of NH_4^+, produced during organic matter degradation, substituting for K^+ and Na^+ (Ramseyer et al., 1993; Orberger et al., 2005).

Bulk Geochemistry

The major element composition of the vent samples compares well with the petrography. At Tom, Fe_2O_3, MnO, MgO and CaO display large increases above NASC, corroborating the extensive alteration associated with Stage 1 mineralisation. This pattern is not observed at Nidd, indicating the lack of ankerite and pyrite within the vent here. For both Tom and Nidd samples, Al_2O_3, Na_2O, K_2O and TiO_2 display marked decreases below NASC. This may reflect the release of these elements during the alteration of aluminosilicate phases within the host rock.

Apart from a positive Eu anomaly, which may be produced by Ba-feldspar within the samples, the similarity of the REE profile with PAAS and un-mineralised Selwyn Basin shale samples may be a reflection of the paleohydrology of the system. It is likely that hydrothermal fluids equilibrated with either strata underlying, or host to, the developing mineralisation system. This may have important consequences for the bulk geochemistry and redox state of the metal transporting fluid (Cooke *et al.*, 2000; Tornos and Heinrich, 2008).

A scenario involving the upflow of a hydrothermal fluid through a package of basinal strata does not directly conflict with previous suggestions for the source of the metals. Hyland Group rocks that form the oldest exposed rocks in the Selwyn Basin are considered to be a source of Pb and Zn from Fe-oxide coatings of detrital minerals (Goodfellow and Lydon, 2007). However it may be necessary to consider an alternative model involving the dewatering of saline pore fluids from metal-rich, organic-poor pyritic shale; this has been suggested as a mechanism by which to generate sulphur-deficient, base metal enriched brines (Tornos and Heinrich, 2008).

CONCLUSIONS

It is suggested that future fluid inclusion studies focus on sampling siderite, quartz (Qz-II), Ba-carbonates and sphalerite from Stage 2. In terms of stratabound mineralisation, it is clear that the majority of textures, when considered carefully at both the hand sample and microscopic scale, do not provide convincing evidence for syn-sedimentary mineralisation. Barite and sulphide minerals occur independently of each other during Stage 2 and it is possible that Stage 2 mineralisation took place below the SWI in a diagenetic environment. This raises the question of whether euxinic conditions in the marine environment are a necessary component of the model for mineralisation (e.g. Goodfellow and Lydon, 2007).

The results of bulk geochemistry indicate that the hydrothermal fluid was enriched in Au, which raises questions of source and transport mechanisms. The general correlation of the REE profile with the NASC indicates the hydrothermal fluid likely equilibrated with either underlying basinal strata.

Future work should concentrate on fluid inclusion analysis of mineral phases more closely associated with the ore-forming phases; assessing the geochemistry of background strata to determine the redox state of the basin during mineralisation; and sampling the Pb and Sr isotopes of suitable vent mineral phases to further evaluate the paleohydrology of the system.

REFERENCES

Abbott, J.G., 1982. Structure and stratigraphy of the MacMillan Fold Belt; evidence for Devonian faulting: *in* Yukon Geology and Exploration-1981; Exploration and Geological Services Division, Yukon, Indian and Northern Affairs Canada, p. 22-33.

Abbott, J.G., and Turner, R.J.W., 1990. Character and Paleotectonic Setting of Devonian Sediment-Hosted Zn-Pb-Barite Deposits, Macmillan Fold Belt, Yukon: *in* Abbott, J.G., and Turner, R.J.W., eds., Mineral deposits of the northern Canadian Cordillera: Ottowa, International Association on the Genesis of Ore Deposits, Eighth Symposium, Field Trip 14 Guidbook, p. 99-136.

Ansdell, K.M., Nesbitt, B.E., and Longstaffe, F.J., 1989. A fluid inclusion and stable-isotope study of the Tom Ba-Pb-Zn deposit, Yukon Territory, Canada; Economic Geology, v. 84, p. 841-856.

Dellwig, O., Hinrichs, J., Hild, A., and Brumsack, H.-J., 2000. Changing sedimentation in tidal flat sediments of the southern North Sea from the Holocene to the present: a geochemical approach; Journal of Sea Research, v. 44, p. 195-208.

Dickinson, W.R., 2004. Evolution of the North American Cordillera; Annual Review of Earth and Planetary Sciences, v. 32, p. 13-45.

Eisbacher, G.H., 1985. Late Proterozoic Rifting, Glacial Sedimentation, and Sedimentary Cycles in the Light of Windermere Depostion, Western Canada, v. 51, p. 231-254.

Essene, E.J., Claflin, C.L., Giogetti, G., Mata, P.M., Peacor, D.R., Arkai, P., and Rathmell, M.A., 2005, Two-, three- and four-feldspar assemblages with hyalophane and celsian: implications for phase equilibria in $BaAl_2Si_2O_8$-$CaAl_2Si_2O_8$-$NaAlSi_3O_8$-$KAlSi_3O_8$: European Journal of Mineralogy, v. 17, p. 515-535.

Fernandes, N.A., 2011. Geology and Geochemistry of Late Devonian-Mississipian Sediment-Hosted Barite Sequences of the Selwyn Basin, NWT and Yukon, Canada; MSc thesis, University of Alberta.

Gabrielse, H., 1967. Tectonic Evolution of the Northern Canadian Cordillera; Canadian Journal of Earth Sciences, v. 4, p. 271-300.

Gardner, H.D., and Hutcheon, I., 1985. Geochemistry, Mineralogy, and Geology of the Jason Pb-Zn Deposits, Macmillan Pass, Yukon, Canada; Economic Geology, v. 80, p. 1257-1276.

Goodfellow, W.D. and Jonasson, I.R., 1984. Ocean stagnation and ventilation defined by secular trends in pyrite and barite, Selwyn Basin, Yukon; Geology, v. 12, p. 583-586.

Goodfellow, W.D., Lydon, J.W., and Turner, R.J.W., 1993. Geology and genesis of sediment-hosted (SEDEX) zinc-lead-silver sulphide deposits; Geological Association of Canada Special Paper 40, p. 201-251.

Goodfellow, W.D., Cecile, M.P., and Leybourne, M.I., 1995. Geochemistry, petrogenesis, and tectonic setting of lower Paleozoic alkali and potassic volcanic rocks, Northern Canadian Cordilleran Miogeocline; Canadian Journal of Earth Sciences, v. 32, p. 1236-1254.

Goodfellow, W.D., 2007. Base metal metallogeny of the Selwyn Basin, Canada, *in* Goodfellow, W.D., ed., Mineral Deposits of Canada: A Synthesis of Major Deposit Types, District Metallogeny, the Evolution of Geological Provinces, and Exploration Methods: Geological Association of Canada, Mineral Deposits Division, Special Publication No. 5, p.553-579.

Gordey, S.P., Abbott, J.G., and Orchard, M.J., 1982. Devono-Mississippian Earn Group and younger in strata in east-central Yukon: Current Research, Part B; Geological Survey of Canada, Paper 82-1B, p. 93-100.

Gordey, S.P., and Anderson, R.G., 1993. Evolution of the northern Cordilleran Miogeocline, Nahanni map area (105I), Yukon and Northwest Territories, Geological Survey of Canada, Memoir 428, 214 p.

Gordey, S.P., Macdonald, J.D., Turner, E.C., and Long, D.G.F., 2010. Chapter 5. Structural Geology of the Central Mackenzie Mountains; *in* Geology of the central Mackenzie Mountains of the northern Canadian Cordillera, Sekwi Mountain (105P), Mount Eduni (106A), and northwestern Wrigley Lake (95M) map-areas, Northwest Territories; Martel, E., Turner, E.C., and Fischer, B.J. (editors), NWT Special Volume 1, NWT Geoscience Office, p. 193-214.

Griffith, E.M., and Paytan, A., 2012. Barite in the ocean – occurrence, geochemistry and palaeoceanographic applications; Sedimentology, v. 59, p. 1817-1835.

Gromet, L.P., Dymek, R.F., Haskin, L.A., and Korotev, R.L., 1984. The "North American shale composite": Its compilation, major and trace element characteristics: Geochimica et Cosmochimica Acta, v. 48, p. 2469-2482.

Hart, C.J.R., Goldfarb, R.J., Lewis, L.L., and Mair, J.L., 2004. The Northern Cordilleran Mid-Cretaceous Plutonic Province: Ilmenite/Magnetite-series Granitoids and Intrusion-related Mineralisation; Resource Geology, v. 54, p. 253-280.

Hendy, I.L., 2010. Diagenetic behavior of barite in a coastal upwelling setting; Paleoceanography, v. 25, p. 1-9.

Henkel, S., Mogollon, J.M., Nothen, K., Franke, C., Bogus, K., Robin, E., Bahr, A., Blumenberg, M., Pape, T., Seifert, R., Marz, C., Lange, G.J., and Kasten, S., 2012. Diagenetic barium cycling in Black Sea sediments – A case study for anoxic marine environments; Geochimica et Cosmochimica Acta, v. 88, p. 88-105.

Irwin, S.E.B., and Orchard, M.J., 1991. Upper Devonian-Lower Carboniferous conodont biostratigraphy of the Earn Group and overlying units, northern Canadian Cordillera, *in* Orchard, M.J., and McCracken, A.D., eds. Ordovician to Triassic Conodont Paleontology of the Canadian Cordillera; Geological Survey of Canada, Bulletin 417, p. 185-213.

Lund, K., 2008. Geometry of the Neoproterozoic and Paleozoic rift margin of western Laurentia: Implications for mineral deposit settings; Geosphere, v. 4, p. 429-444.

Macquaker, J.H.S., Bentley, S.J., and Bohacs, K.M., 2010. Wave-enhanced sediment-gravity flows and mud dispersal across continental shelves: Reappraising sediment transport processes operating in ancient mudstone successions; Geology, v. 38, p. 947-950.

Magnall, J.M., and Gleeson, S.A., 2012a. Macmillan Pass – Tom Deposit; Unpublished Report – Geological Survey of Canada, 14p.

Magnall, J.M., and Gleeson, S.A., 2012b. Boundary Creek (Nidd); A Preliminary Petrographical Assessment: Unpublished Report – Geological Survey of Canada, 17p.

McDonough, W.F., and Sun, S.-s., 1995. The Composition of the Earth; Chemical Geology, v. 120, p. 223-253.

McLennan, S.M., 1989. Rare earth elements in sedimentary rocks; influence of provenance and sedimentary processes; Reviews in Mineralogy and Geochemistry, v. 21, p. 169-200.

McLennan, S.M., 2001. Relationships between the trace element composition of sedimentary rocks and upper crust; Geochemistry, Geophysics, Geosystems, v. 2.

Moro, M.C., Cembranos, M.L., and Fernandez, A., 2001. Celsian, (Ba,K)-Feldspar and Cymrite from Sedex Barite Deposits of Zamora, Spain; The Canadian Mineralogist, v. 39, p. 1039-1051.

Nelson, J., Paradis, S., Christensen, J., and Gabites, J., 2002. Canadian Cordilleran Mississippi Valley-Type Deposits: A Case for Devonian-Mississippian Back-Arc Hydrothermal Origin; Economic Geology, v. 97, p. 1013-1036.

Nelson, J., and Colpron, M., 2007. Tectonics and metallogeny of the British Columbia, Yukon and Alaskan Cordillera, 1.8Ga to the present, *in* Goodfellow, W.D., ed., Mineral Deposits of Canada: A Synthesis of Major Deposit-Types, District Metallogeny, the Evolution of Geological Provinces, and Exploration Methods: Geological Association of Canada, Mineral Deposits Division, Special Publication No. 5, p. 755-791.

Orberger, B., Gallien, J.P., Pinti, D.L., Fialin, M., Daudin, L., Grocke, D.R., and Pasava, J.P., 2005. Nitrogen and carbon partitioning in diagenetic and hydrothermal mineral from Paleozoic Black Shales, (Selwyn Basin, Yukon Territories, Canada); Chemical Geology, v. 218, p. 249-264.

Paytan, A., Mearon, S., Cobb, K., and Kastner, M., 2002. Origin of marine barite deposits: Sr and S isotope characterization; Geology, v. 30, no. 8, p. 747-750.

Paytan, A., Martinez-Ruiz, F., Eagle, M., Ivy, A., and Wankel, S.D., 2004. Using sulphur isotopes to elucidate the origin of barite associated with high organic matter accumulation events in marine sediments; Geological Society of America, Special Paper 379, p. 151-160.

Ramseyer, K., Diamond, L.W., and Boles, J.R., 1993. Authigenic K-NH_4-Feldspar in Sandstones: A Fingerprint of the Diagenesis of Organic Matter; Journal of Sedimentary Petrology, v. 63, p. 1092-1099.

Schieber, J., Southard, J.B., and Schimmelmann, A., 2010. Lenticular Shale Fabrics From Intermittent Erosion of Water-Rich Muds – Interpreting the Rock Record in the Light of Recent Flume Experiments; Journal of Sedimentary Research, v. 80, p.119-128.

Schieber, J., 2011. Reverse engineering mother nature – Shale sedimentology from an experimental perspective; Sedimentary Geology, v. 238, p. 1-22.

Thiessen, E.J., Gleeson, S.A., Dufrane, S.A., Carne, R.C., and Dumala, M., 2012. Upper age constraint and paragenesis of the Tiger Zone, Rau property, central Yukon. *In:* Yukon Exploration and Geology 2011, K.E. MacFarlane and P.J. Sack (eds.), Yukon Geological Survey, p. 151-164.

Tornos, F. and Heinrich, C.A., 2008. Shale basins, sulfur-deficient ore brines and the formation of exhalative base metal deposits. Chemical Geology, v. 247, p. 195–207.

	As	Pb	S	Fe	Bi	Sb	Cu	Ag	W	Zn	TOTALS
						Pyrite					
N	30	32	32	32	32	9	13	15	3	6	
Mean (wt. %)	0.16	0.26	52.67	45.79	0.18	0.02	0.09	0.03	0.03	0.04	**99.27**
Max	0.74	0.46	53.50	46.46	0.24	0.03	0.37	0.06	0.04	0.08	
Min	0.01	0.12	52.01	45.38	0.13	0.01	0.01	0.02	0.02	0.01	
% Std Dev	118.0	27.8	0.7	0.5	16.3	22.9	133.7	41.5	25.1	60.8	
						Pyrrhotite					
N	8	9	10	10	10	2	2	6	2	1	
Mean (wt. %)	0.04	0.19	39.16	59.57	0.15	0.02	0.03	0.02	0.03	0.03	**99.22**
Max	0.05	0.33	39.33	59.81	0.18	0.02	0.03	0.02	0.03	0.03	
Min	0.03	0.07	38.89	59.18	0.09	0.01	0.02	0.02	0.03	0.03	
% Std Dev	13.7	39.6	0.4	0.3	20.2	37.1	25.5	15.7	0.0	0.0	
						Chalcopyrite					
N	9	17	19	19	19	4	19	14			
Mean (wt. %)	0.04	0.17	34.59	29.69	0.13	0.02	35.05	0.06			**99.75**
Max	0.07	0.33	35.10	29.97	0.21	0.02	35.43	0.11	< D.L		
Min	0.01	0.09	34.03	29.32	0.08	0.01	34.64	0.03			
% Std Dev	37.9	36.0	0.7	0.6	31.2	18.5	0.5	47.7			
						Sphalerite					
N	5	8	9	9	9	2	4	5		9	
Mean (wt. %)	0.04	0.22	33.42	7.62	0.14	0.02	0.07	0.04		58.93	**100.49**
Max	0.08	0.37	33.91	8.31	0.18	0.02	0.22	0.05	< D.L	61.13	
Min	0.02	0.10	32.88	6.82	0.12	0.02	0.02	0.02		58.22	
% Std Dev	47.8	45.6	1.1	5.5	14.7	17.9	115.4	28.0		1.4	
						Galena					
N	5	9	9	6	9	9	1	1		3	
Mean (wt. %)	0.03	85.95	13.19	0.06	0.19	0.05	0.18	0.03		0.02	**99.68**
Max	0.03	86.67	13.28	0.13	0.29	0.10	0.18	0.03	< D.L	0.03	
Min	0.02	85.14	13.13	0.02	0.10	0.01	0.18	0.03		0.02	
% Std Dev	20.0	0.6	0.4	65.7	31.0	44.2	0.0	0.0		13.4	
						Arsenopyrite					
N	5	4	5	5	5	5	2			1	
Mean (wt. %)	42.84	0.16	22.20	34.60	0.10	0.08	0.02			0.03	**100.03**
Max	43.82	0.28	22.97	34.85	0.15	0.16	0.02	< D.L		0.03	
Min	41.30	0.09	21.87	34.24	0.06	0.04	0.02			0.03	
% Std Dev	2.0	48.4	1.9	0.7	29.1	50.7	11.1			0.0	
Instrumental Detection Limit (3σ)											
ppm	116	639	96	95	241	104	94	138	208	123	
%	0.012	0.064	0.010	0.010	0.024	0.010	0.009	0.014	0.021	0.012	

Table 1. Summary table of EPMA data for sulphides from the vent complex at Tom. Results below a detection limit of 3σ have not been reported and are indicated by < D. L.

	CaO	MgO	FeO	MnO	SrO	BaO	
			Siderite $FeCO_3$				
N	3	3	3	3			
Mean (wt. %)	0.95	2.11	56.92	0.91			
Max	1.31	3.22	57.42	2.23	< D.L		
Min	0.72	0.39	56.42	0.18			
% Std Dev	26.7	58.4	0.7	103.4			
							TOTAL
apfu	0.02	0.06	0.91	0.01			**1.00**
			Calcite $CaCO_3$				
N	18	18	18	18	11	8	
Mean (wt. %)	56.22	0.15	0.52	0.15	0.04	0.09	
Max	57.86	0.32	0.73	0.21	0.15	0.14	
Min	54.52	0.08	0.35	0.11	0.02	0.06	
% Std Dev	1.4	42.8	21.4	16.4	80.6	28.5	
							TOTAL
apfu	0.99	0.00	0.01	0.00	0.00	0.00	**1.00**
			Ankerite $Ca(Mg,Fe^{2+},Mn)(CO_3)_2$				
N	73	73	73	73	54	5	
Mean (wt. %)	27.87	11.74	15.56	0.87	0.40	0.08	
Max	30.16	13.76	19.78	2.35	1.16	0.10	
Min	26.63	9.11	12.06	0.18	0.02	0.07	
% Std Dev	2.7	10.9	12.3	78.3	98.4	12.9	
							TOTAL
apfu	0.49	0.29	0.21	0.01	0.00	0.00	**1.00**
			Barytocalcite $BaCa(CO_3)_2$				
N	60	42	7		60	60	
Mean (wt. %)	17.80	0.03	0.05		0.39	52.86	
Max	18.06	0.12	0.07	< D.L	0.60	53.83	
Min	17.45	0.01	0.03		0.18	51.96	
% Std Dev	0.8	52.6	30.3		19.8	0.8	
							TOTAL
apfu	0.48	0.00	0.00		0.01	0.52	**1.00**
Instrumental Detection Limit							
3σ (ppm)	157	106	329	302	164	632	
%	0.016	0.011	0.033	0.030	0.016	0.063	

Table 2. Summary table of EPMA data for carbonates from the vent complex at Tom. Results below a detection limit of 3σ have not been reported and are indicated by < D. L. *Apfu* = atoms per formula unit.

	SiO_2	Al_2O_3	FeO	MnO	MgO	BaO	CaO	Na_2O	K_2O	
					Celsian $BaAl_2Si_2O_8$					
N	66	66	10	5	45	66	27	66	66	
Mean (wt. %)	34.13	28.74	0.04	0.03	0.02	38.23	0.02	0.14	0.31	
Max	36.19	29.41	0.06	0.04	0.04	39.20	0.07	0.33	1.19	
Min	32.88	27.79	0.03	0.02	0.01	36.35	0.01	0.05	0.04	
% Std Dev	2.32	1.07	28.03	21.71	41.71	2.10	56.06	33.52	79.05	
										TOTAL
apfu	*2.03*	*2.02*	*0.00*	*0.00*	*0.00*	*0.89*	*0.00*	*0.02*	*0.02*	***4.98***
					Hyalophane $(K,Ba)Al(Si,Al)_3O_8$					
N	10	10	3	1	9	10	4	10	10	
Mean (wt. %)	48.99	23.06	0.04	0.03	0.03	20.49	0.03	0.25	6.55	
Max	49.79	23.87	0.06	0.03	0.05	22.04	0.06	0.34	6.97	
Min	47.64	22.63	0.03	0.03	0.01	19.35	0.01	0.13	5.82	
% Std Dev	1.52	1.44	30.07	0.00	36.95	4.55	72.17	25.52	5.37	
										TOTAL
apfu	*2.59*	*1.44*	*0.00*	*0.00*	*0.00*	*0.42*	*0.00*	*0.03*	*0.44*	***4.92***
Instrumental Detection Limit (3σ)										
ppm	122	101	232	203	89	340	111	105	98	
%	0.0122	0.0101	0.0232	0.0203	0.0089	0.034	0.0111	0.0105	0.0098	

Table 3. Summary table of EPMA data for barium feldspars from the stratabound mineralisation at Tom. Results below a detection limit of 3σ have not been reported and are indicated by < D. L. *Apfu* = atoms per formula unit.

		Tom														Nidd		
	Unit	TU68-21	TU70-7	TU70-19	TU70-20	T91.14-10	T91.14-11	TYK1-6	TYK2-14	TYK2-15	TYK2-16	TYK2-17	TYK2-19	TYK2-20	TYK2-21	368a	368b	368c
SiO_2	%	27.64	62.83	1.22	4.9	5.21	32.04	27.35	5.34	4.8	48.02	4.82	8.65	2.23	25.81	34.75	61.82	19.44
Al_2O_3	%	0.38	8.58	0.19	0.72	0.23	1.21	1.27	1.23	1.02	1.19	1.01	1.82	0.31	0.2	2.63	5.3	1.59
$Fe_2O_3(T)$	%	18.51	13.21	47.14	25.56	30.68	29.72	37.75	2.9	37.07	4.93	24.95	12.93	38.62	23.74	7.23	6.1	7.06
MnO	%	0.439	0.351	1.332	1.203	0.952	0.845	1.094	0.153	1.152	0.211	0.888	0.469	1.161	0.758	0.171	0.094	0.095
MgO	%	6.25	1.12	5.36	6	6.45	3.24	2.94	2.14	4.91	0.69	5.11	5.57	6.91	4.42	0.21	0.22	0.18
CaO	%	16.62	0.24	8.85	14.96	14.87	5.8	4.02	10.34	7.88	1.86	12.76	18.59	11.27	12.95	0.18	0.12	0.27
Na_2O	%	0.01	0.06	0.01	0.04	0.01	0.02	0.01	0.07	0.07	0.03	0.04	0.16	0.01	0.02	0.03	0.06	0.03
K_2O	%	0.04	2.31	<0.01	0.05	<0.01	0.03	0.03	0.13	0.1	0.05	0.05	0.16	<0.01	<0.01	0.26	0.5	0.1
TiO_2	%	0.015	0.505	0.001	0.034	0.018	0.071	0.05	0.002	0.006	0.021	0.005	0.008	0.004	0.004	0.208	0.324	0.211
P_2O_5	%	0.06	0.1	<0.01	<0.01	0.01	0.03	0.09	0.01	0.01	<0.01	<0.01	0.03	0.01	0.05	0.11	0.07	0.19
LOI	%	23.37	9.02	18.71	15.97	16.89	19.91	22.48	8.04	24.84	8.34	14.93	24.14	32.3	19.03	10.73	6.08	13.36
Au	ppb	30	11	18	113	22	8	<1	<1	<1	<1	104	19	6	7	<1	<1	21
Ag	ppm	11	0.9	9.7	52.7	44.2	6.3	0.7	116	92.2	253	52.7	94	17.1	43.2	35.6	18.5	96.3
As	ppm	88	30	2470	793	453	90	207	70	69	33	759	72	22	110	128	106	150
Ba	ppm	376	5950	1527	10920	21500	12500	9757	308600	957	19610	21360	87040	765	1251	429	1033	142
Be	ppm	<1	2	<1	<1	<1	<1	<1	<1	<1	<1	<1	<1	<1	<1	<1	<1	<1
Bi	ppm	<0.1	0.1	<0.1	0.3	0.2	0.2	<0.1	<0.1	<0.1	0.3	0	<0.1	<0.1	<0.1	0.1	0.2	0.2
Br	ppm	3.2	2.2	<0.5	<0.5	<0.5	<0.5	2.8	<0.5	3.9	<0.5	<0.5	4.3	3.3	2.7	3.2	3.7	5.5
Cd	ppm	2	0.6	35.7	157	40.3	1.2	2.8	71.1	96.5	226	239	5.7	9.4	7.2	929	7.7	52.7
Co	ppm	23.6	15.7	23.7	86.9	21.9	16.6	13.7	4	10	20.8	192	5.1	3.2	8.7	309	5.7	69.2
Cr	ppm	8.8	82	<0.5	14.8	16.1	38.8	29.4	<0.5	10	7.3	9.6	<0.5	24.2	9.2	1300	11.9	30.9
Cs	ppm	0.2	5.3	<0.1	0.2	<0.1	0.4	0.2	0.3	0.3	0.4	0.2	0.5	<0.1	<0.1	1	1.6	0.8
Cu	ppm	6520	61	600	167	337	227	103	3	125	926	3600	80	2320	3980	405	263	1390
Ga	ppm	<1	15	2	7	3	3	4	3	3	14	6	3	2	1	28	13	25
Ge	ppm	2	4.6	2.3	9.9	13.6	8.1	8.5	24.3	7	100	25.4	1.4	1.8	15.5	156	111	323
Hf	ppm	0.2	2.8	<0.1	0.4	0.2	0.5	0.1	0.4	0.2	0.2	0.1	0.5	<0.1	<0.1	1.2	1.6	1.3
Hg	ppm	<1	<1	3	4	7	<1	<1	5	5	10	23	<1	<1	<1	203	92	278
In	ppm	0.2	0.1	0.3	0.6	0.2	0.2	0.1	0.2	0.5	2.7	0.8	0.1	0.2	0.3	0.6	0.2	0.4
Ir	ppb								<1								<1	
Mo	ppm	<2	4	<2	<2	2	5	3	<2	<2	3	<2	<2	<2	<2	2	4	4
Nb	ppm	0.4	199	<0.2	185	2.4	90.9	3.5	12.1	1.2	74.2	1	16.5	<0.2	26.5	7.4	9.5	7.9
Ni	ppm	78	71	57	72	24	25	19	1	14	33	216	5	6	14	27	29	39
Pb	ppm								>5000							587	491	3260
Rb	ppm	1	88	<1	4	<1	1	<1	9	7	2	3	11	<1	<1	11	20	5
S	%	2.12	0.715	8.87	14.2	17.6	2.64	0.412	2.19	2.35	5.31	10	2.24	1.11	9.16	12.9	5.24	16.8
Sb	ppm	1.5	4.7	19.1	116	150	23.5	3.1	160	110	277	95.6	112	14.9	65.3	56.1	27.1	235
Sc	ppm	3.52	12.1	1.58	5.39	2.25	4.25	2.72	0.72	2.57	3.45	2.38	1.33	3.72	3.82	4.27	5.96	3.5
Se	ppm	7.8							<0.5							< 0.5	< 0.5	< 0.5
Sn	ppm	21	29	5	52	6	17	3	14	12	52	56	14	12	53	50	11	26
Sr	ppm	272	23	368	970	1107	194	98	1272	66	210	608	10670	296	2463	44	67	50
Ta	ppm	0.3	83.7	0.51	69.2	0.57	36.3	0.24	4.75	0.51	29.6	0.31	6.12	0.14	10.9	2.46	2.71	1.88
Th	ppm	0.24	7.67	< 0.05	0.69	0.26	1.26	0.7	0.67	0.55	0.4	0.21	0.94	0.14	0.11	3.35	4.9	3.69
U	ppm	1.36	3.37	0.05	0.97	0.7	1.23	0.65	0.5	0.39	0.55	0.29	0.8	0.47	0.41	1.53	2.36	1.69
V	ppm	46	282	85	164	153	214	199	37	105	72	95	46	144	87	84	151	57
W	ppm								<1								<1	
Y	ppm	23	19	4	11	7	8	5	10	4	5	6	12	19	14	10	13	12
Zn	ppm	6730	38	8140	31400	7560	121	566	8330	18700	48100	66900	216	1750	949		88100	
Zr	ppm	7	109		13	8	17	10	6	5	8	5	17	2	2	49	68	58
La	ppm	1.66	34.6	0.14	0.91	1.18	4.46	7.35	3.27	0.89	0.71	1.12	2.18	0.32	0.52	13.9	20.4	14.7
Ce	ppm	3.06	57	0.51	1.94	2.52	8.41	13.3	1.43	1.55	1.27	1.72	2.76	0.97	1.82	25.7	37.5	27.5
Pr	ppm	0.42	6.75	0.1	0.35	0.4	1.36	1.99	0.35	0.31	0.17	0.31	0.57	0.2	0.44	3.14	4.75	3.47
Nd	ppm	1.52	23.2	0.65	1.41	1.91	5.85	7.52	1.31	1.4	0.8	1.25	2.33	0.94	2.69	11.7	17.3	14.4
Sm	ppm	0.9	3.66	0.47	0.88	0.99	1.52	1.53	1	0.56	0.43	0.72	1.04	0.73	1.92	2.98	4.02	3.35
Eu	ppm	0.578	0.964	1.12	1.85	2	0.92	1.56	0.757	0.806	0.574	1.76	2.33	1.28	2.01	1.68	1.91	1.84
Gd	ppm	3.57	2.72	0.96	1.93	1.84	1.41	1.36	2.69	0.96	0.93	1.47	2.14	3.33	3.01	2.47	2.39	3.31
Tb	ppm	0.74	0.47	0.2	0.34	0.31	0.26	0.2	0.32	0.2	0.16	0.27	0.37	0.77	0.61	0.35	0.33	0.49
Dy	ppm	4.46	3.21	1.24	2.13	1.76	1.75	1.01	1.55	1.27	0.91	1.56	2.14	4.8	3.37	1.91	2.12	2.75
Ho	ppm	0.81	0.69	0.24	0.42	0.29	0.38	0.19	0.28	0.24	0.18	0.29	0.38	0.81	0.56	0.37	0.45	0.51
Er	ppm	2.15	2.15	0.7	1.17	0.74	1.14	0.51	0.79	0.66	0.5	0.81	1.07	1.75	1.29	1.08	1.37	1.4
Tl	ppm	<0.05	1.37	<0.05	<0.05	<0.05	<0.05	0.07	<0.05	<0.05	0.12	<0.05	<0.05	<0.05	<0.05	0.16	0.88	0.08
Tm	ppm	0.311	0.329	0.104	0.17	0.095	0.168	0.073	0.116	0.104	0.07	0.114	0.172	0.205	0.156	0.156	0.204	0.2
Yb	ppm	1.89	2.34	0.7	1.1	0.54	1.07	0.44	0.82	0.77	0.44	0.71	1.29	1.12	0.88	1.02	1.37	1.29
Lu	ppm	0.279	0.382	0.105	0.182	0.088	0.165	0.074	0.129	0.133	0.07	0.108	0.219	0.173	0.131	0.159	0.222	0.204
TOTAL		96.9	99.8	93.0	88.2	96.1	96.9	98.6	64.4	86.3	77.7	84.0	84.6	94.5	97.1	69.9	95.0	60.0

Table 4. Major, minor and trace element results from Tom and Nidd vent complex samples. Results below detection or out of analytical range indicated by < or > symbol.

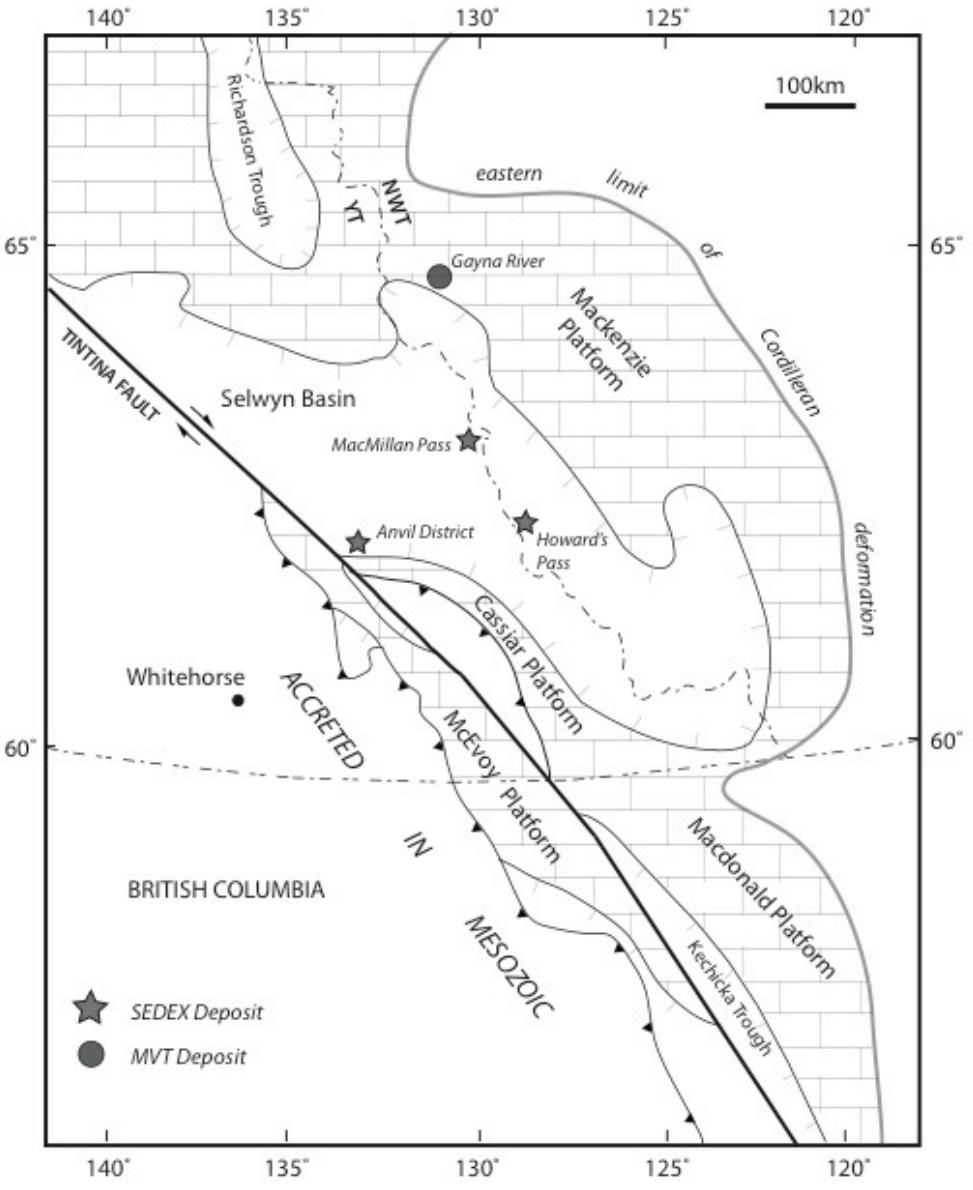

Figure 1. Regional geological setting of the Selwyn Basin and the location of Macmillan Pass. Early Silurian Selywn Basin sediments host SEDEX mineralisation at Howards Pass. Figure modified from Gordey and Anderson, (1993); Goodfellow, (2007); Nelson and Colpron, (2007).

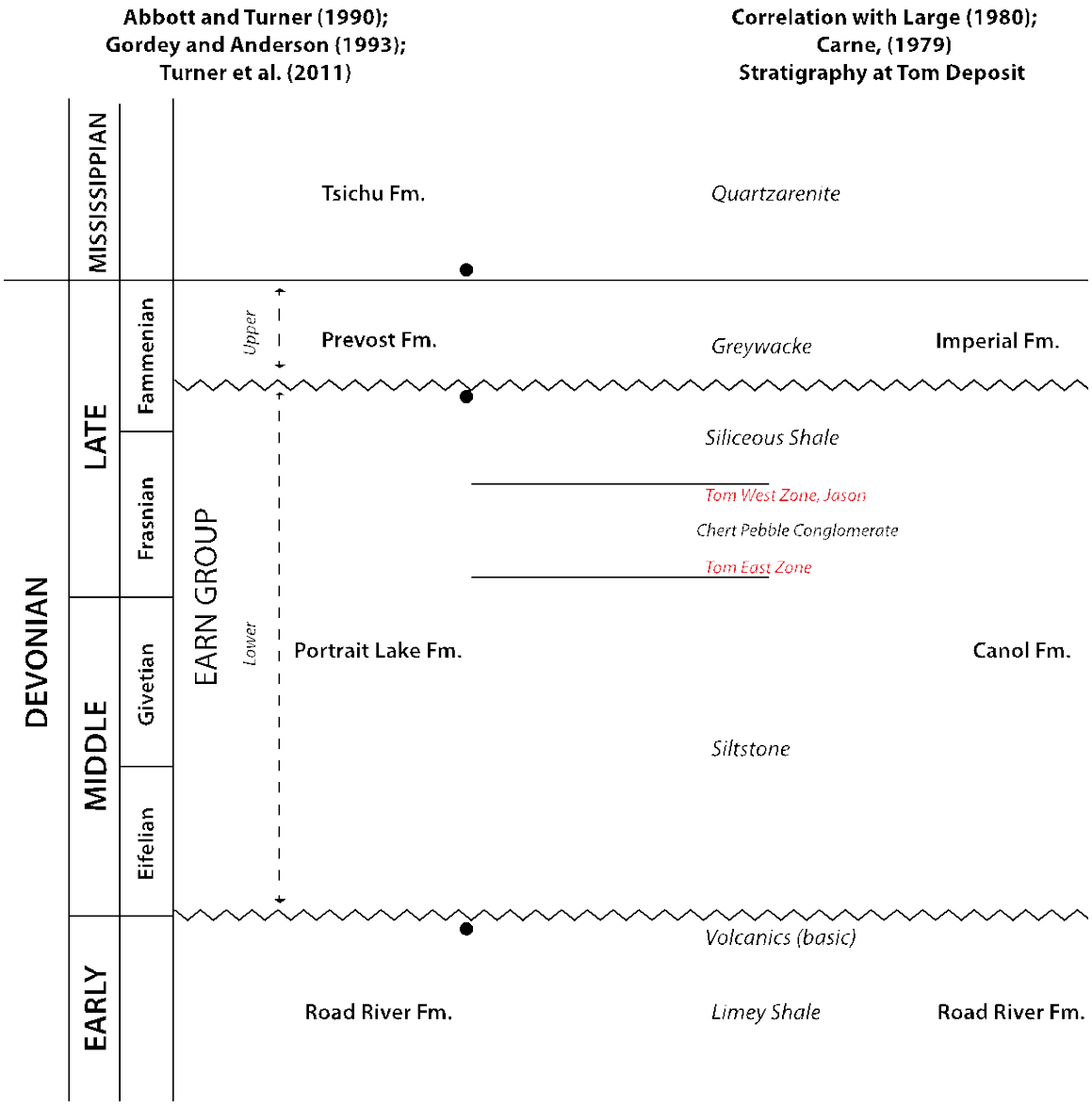

Figure 2. The stratigraphy of Earn Group sediments at Macmillan Pass. Figure modified from Large (1980).

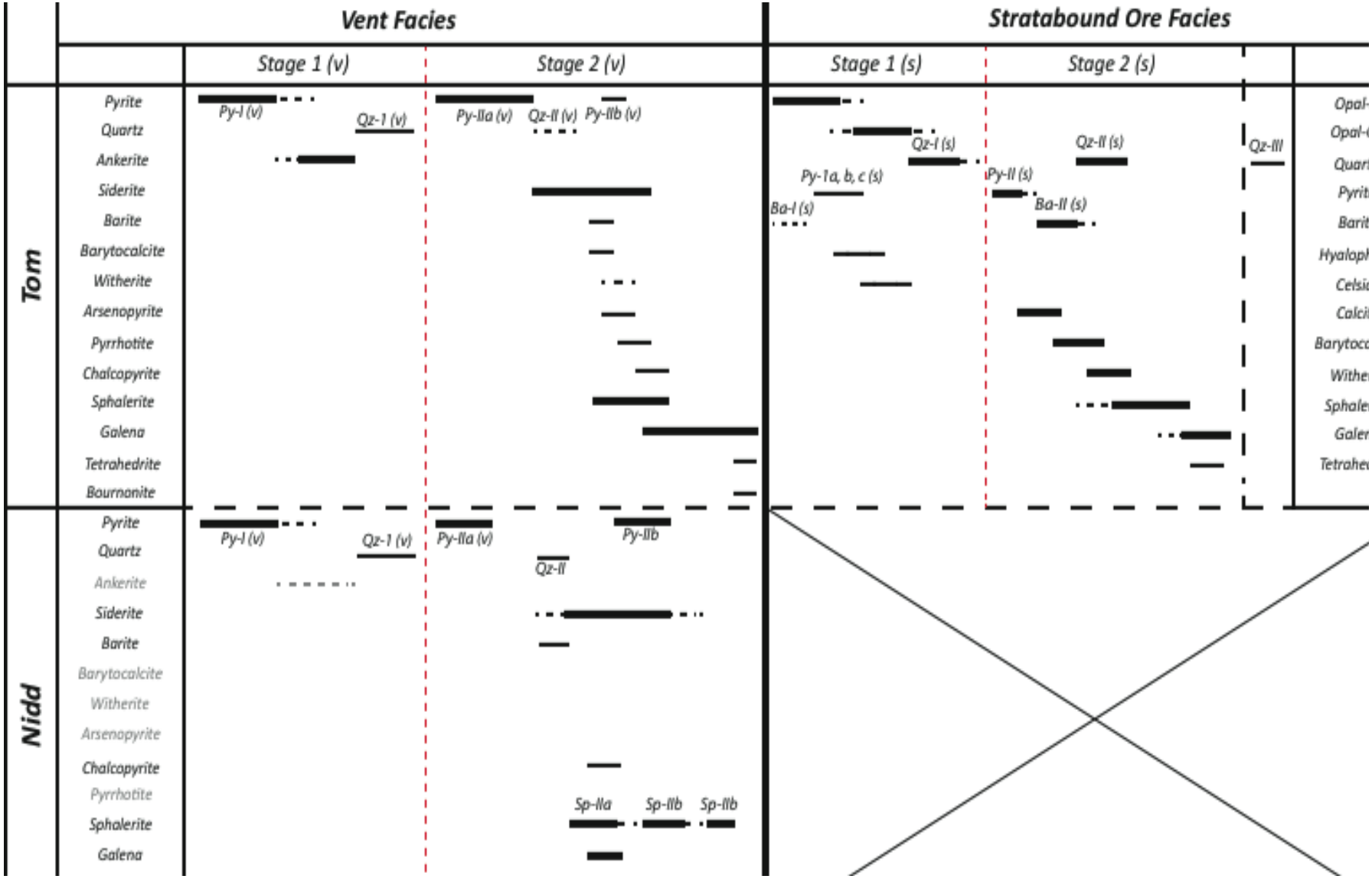

Figure 3. Summary paragenetic sequence for vent complex and stratiform ore mineralization at Tom and Nidd. Minerals are listed down the sides of the figure. Minerals in light grey text at Nidd are present at Tom but absent at Nidd.

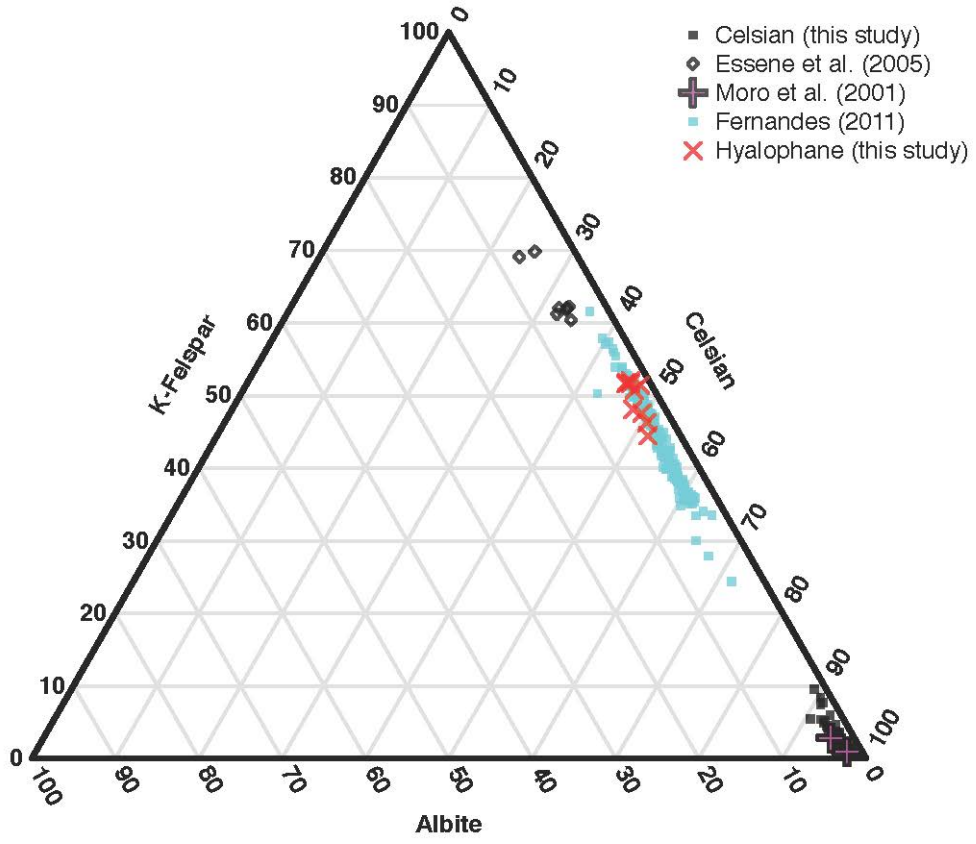

Figure 4. Ternary plot of feldspar composition with Celsian (Ba), Albite (Na) and K-feldspar (K) end-member compositions.

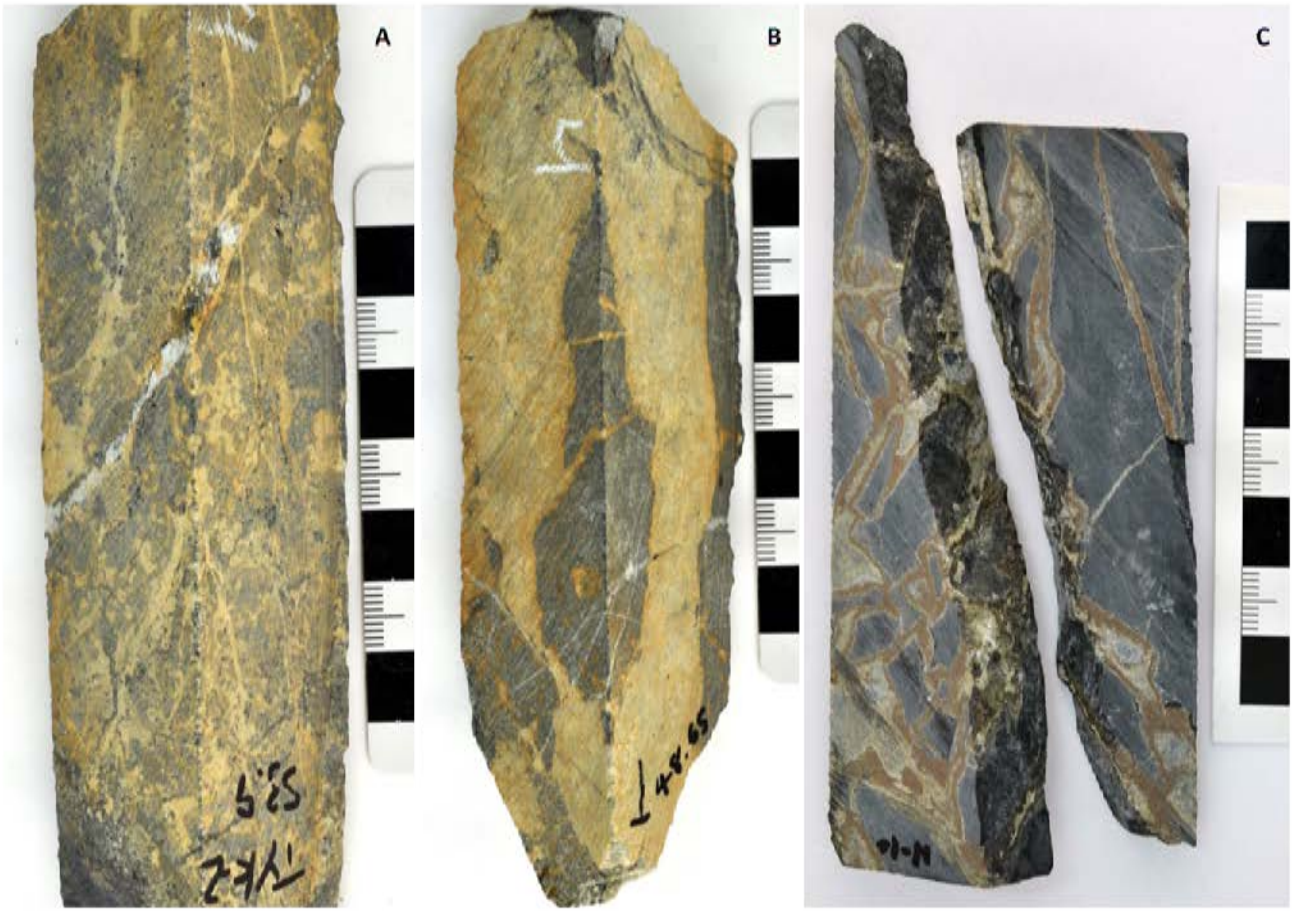

Figure 5. Hand samples from the vent complex of Tom (A and B) and Nidd (C). Scale on right hand side of each is in centimeters.

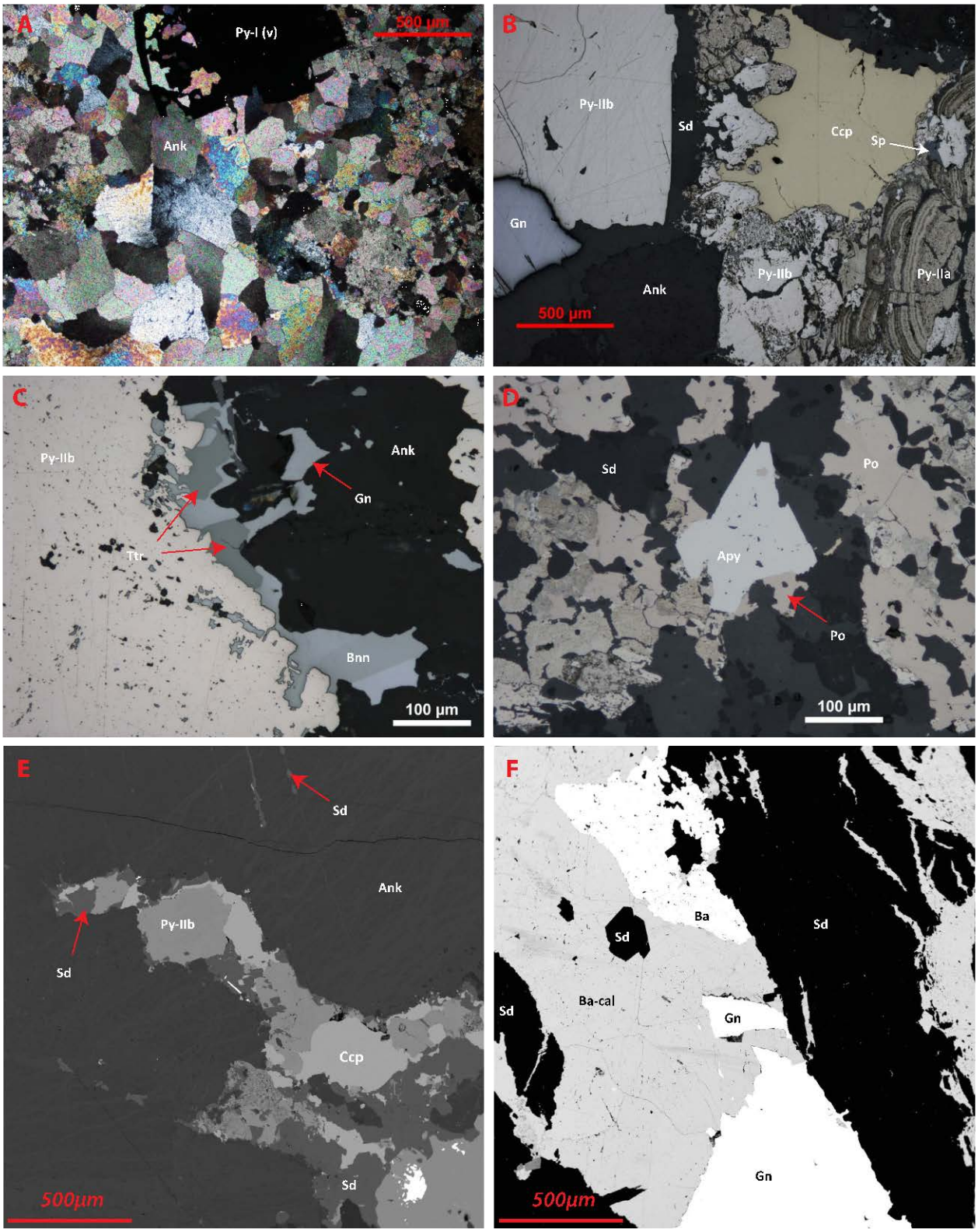

Figure 6. A – *Stage 1* mineralisation (*TYK2-20a; cross-polarized light*); **B** – Sulphide mineralization from *Stage 1* and *2* (*TU.70-2; reflected light*); **C** –*Stage 2* sulphosalt bearing, replacement style galena mineralisation (*TYK1-5; reflected light*); **D** – arsenopyrite and extensive pyrrhotite replacement of pyrite (Py-IIa) (*TU.70-2; reflected light*); **E** – *Stage 2* veinlet of siderite and sulphides crosscutting *Stage 1* ankerite (*TU.70-2; BSE*); **F** – Barytocalcite + barite + galena vein crosscutting siderite (*TYK2-14; BSE*). See **Figure 3** for mineral abbreviations.

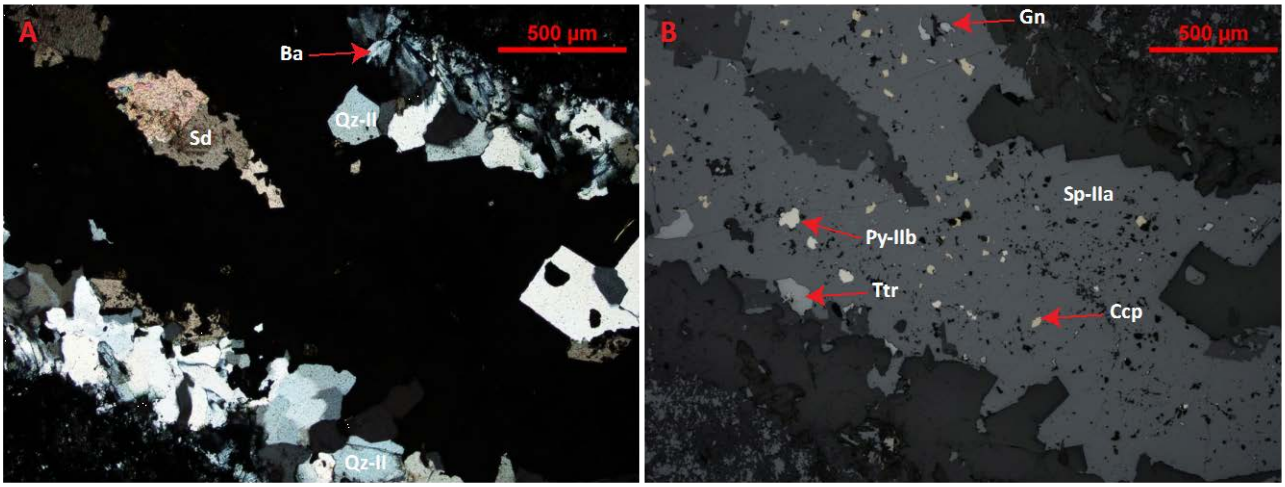

Figure 7. A – vein mineralization in a vent sample from Nidd (*368; cross-polarized light*). Barite and quartz (Qz-II) on vein margin with siderite in center of vein. **B** – reflected light image of **A**. Sphalerite contains inclusions of chalcopyrite, pyrite (Py-IIb), galena and tetrahedrite. See **Figure 3** for mineral abbreviations.

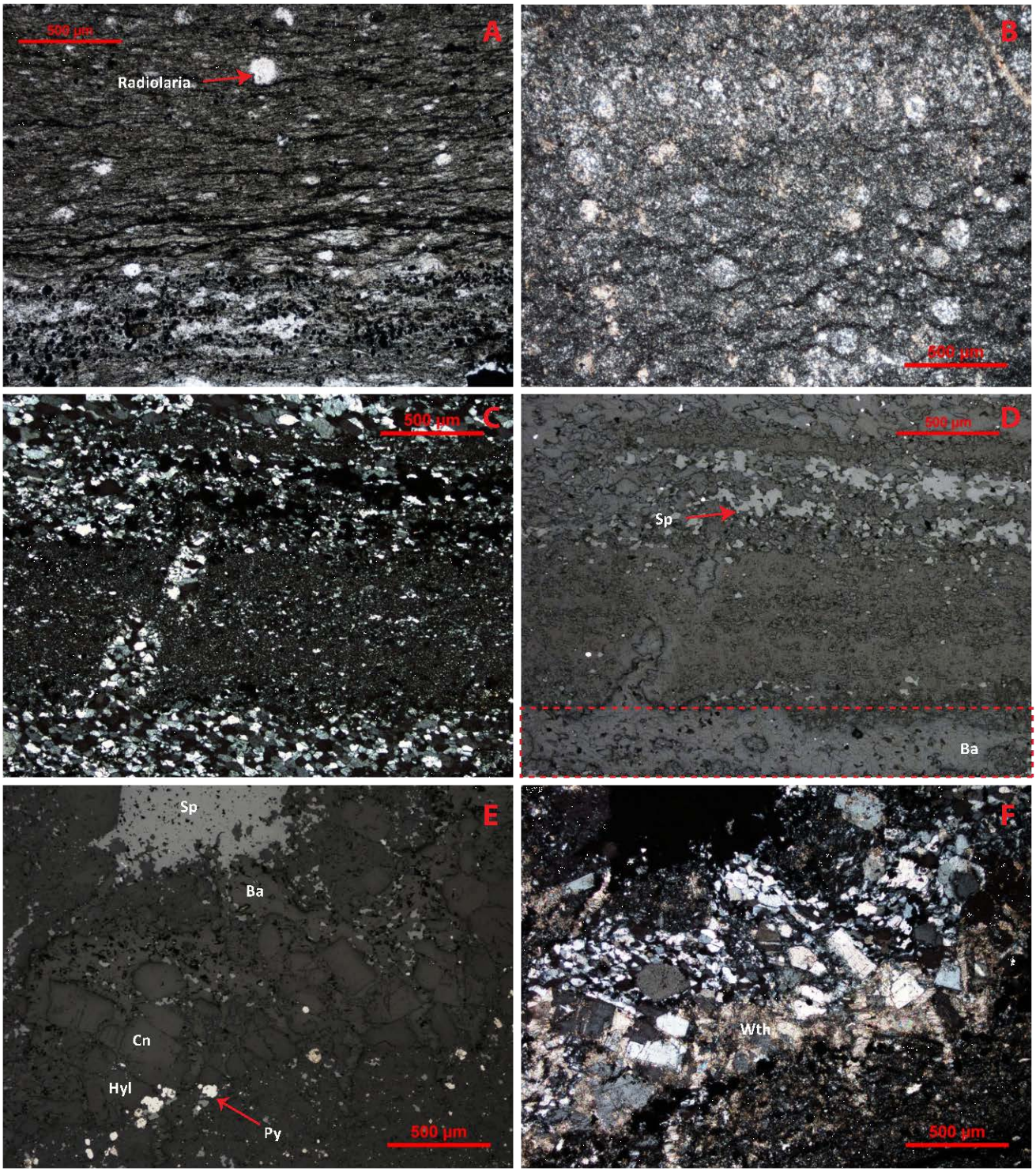

Figure 8. A - Lenticular laminations in clay rich siliceous mudstone (*T91.14-4*; *plane polarized light*). **B** – Recrystallized radiolarians within a calcareous mudstone bed (*TYK2-4a; cross polarized light*). **C** – Siliceous mudstone pseudo-laminated with barite; note the barite veinlet that crosscuts mudstone lamina (*TYK1-4; cross polarized light*). **D** – Reflected light photomicrograph of **C**; **E** – Ba-feldspar horizon above mudstone bed. Ba-feldspar replaced by barite, witherite and sphalerite (*T91.14-5; reflected light*); **F** – cross-polarized image of **E**. See **Figure 3** for mineral abbreviations.

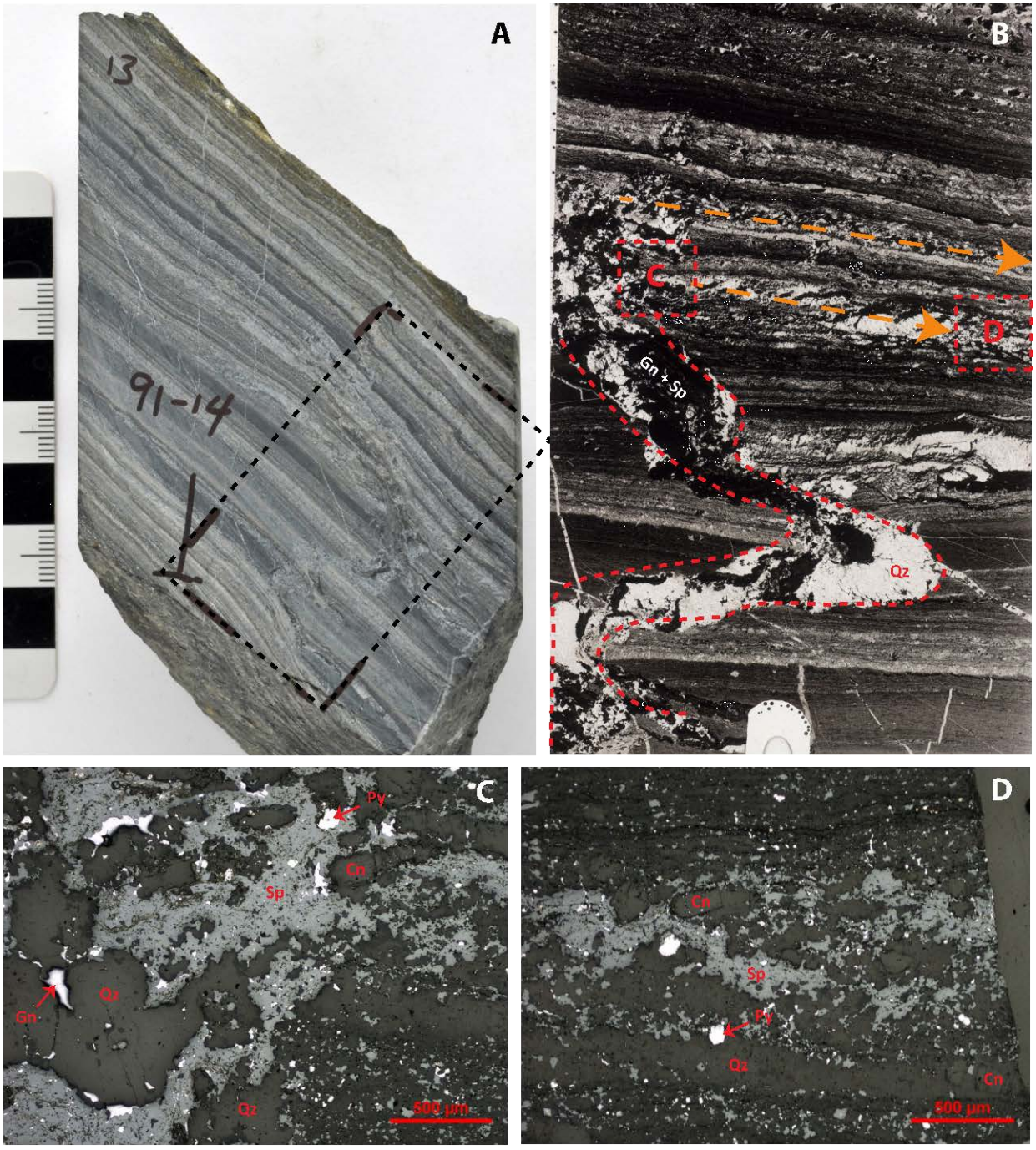

Figure 9. A - Typical hand sample of *Grey Facies* mineralization. Orientated the correct way up. Marked area highlights the area the thin section is cut from. **B** – Thin section scanned image illustrates fine laminations cut by an irregular, sulphide-bearing quartz-carbonate vein that cuts out against overlying laminations (red dashed line), with diffuse replacement of adjacent laminations evident (pink arrows). **C** and **D** – stratal replacement of mudstone lamina by sphalerite, galena and quartz (*T91.14-1; reflected light*). See **Figure 3** for mineral abbreviations.

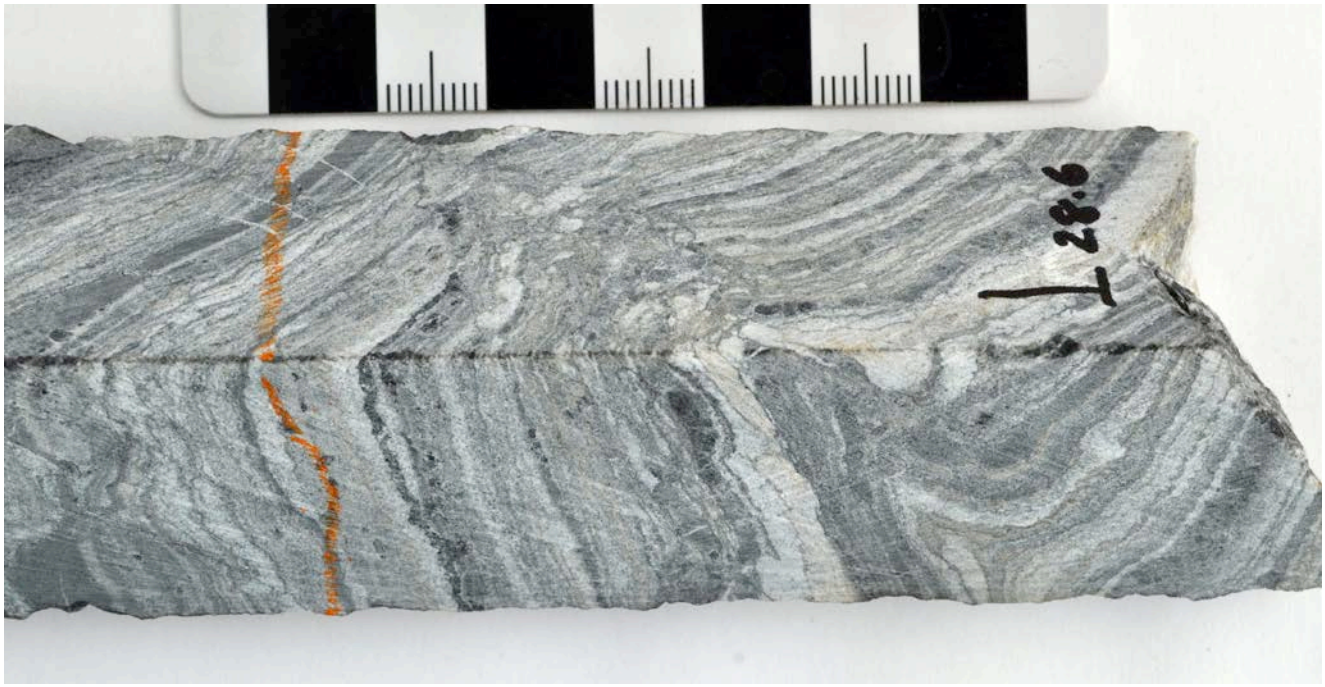

Figure 10. Example of soft sediment deformation (SSD) folding and fluidization in *Grey Facies* sample (*TYK2-7*).

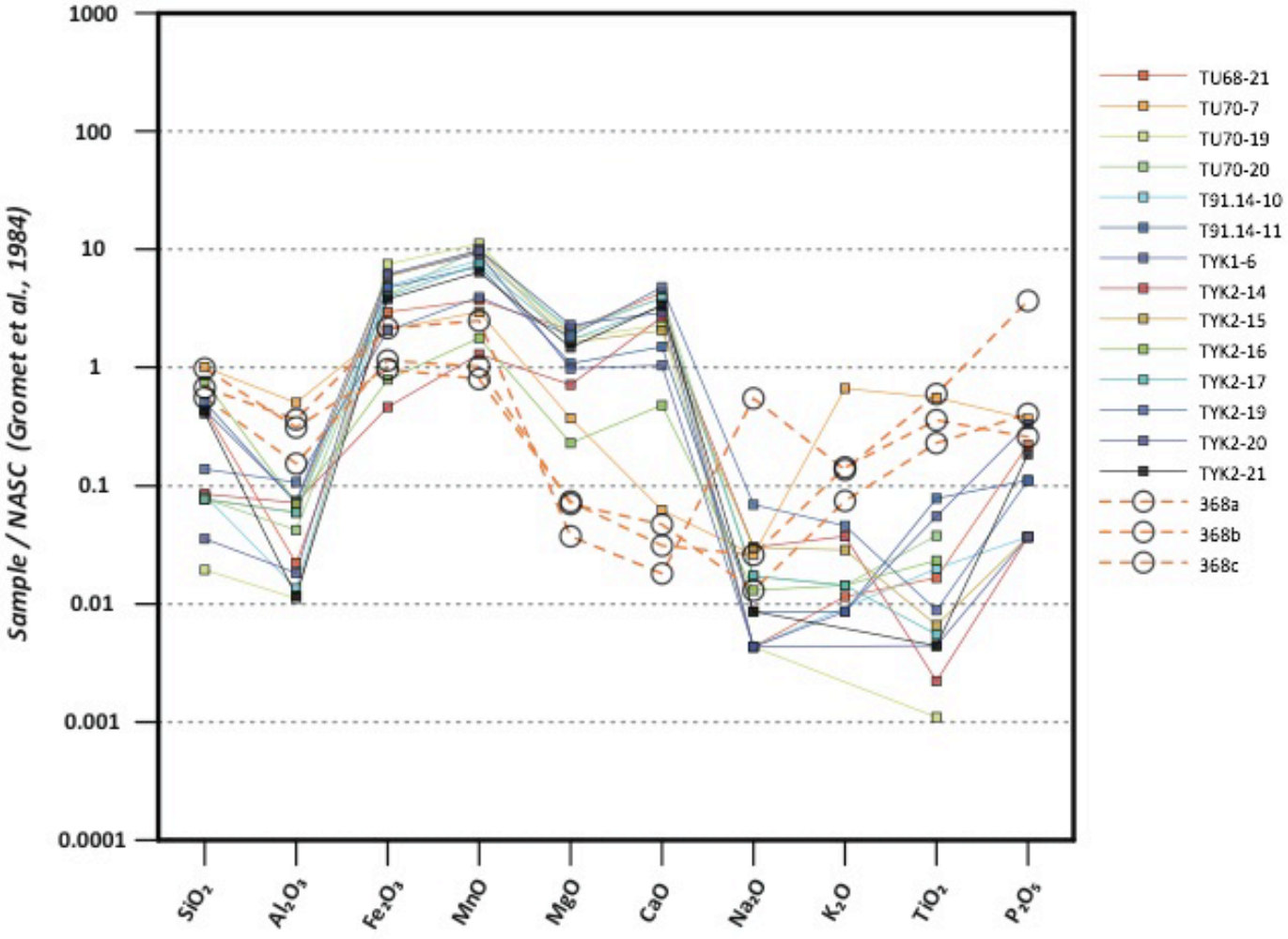

Figure 11. This plot displays the major element oxides of vent samples (Tom, Nidd) normalised to the North American Shale Composite (NASC; Gromet *et al.*, 1984). Samples that plot above the line are enriched relative to the NASC, and samples below are depleted. This provides an indication of the effect of hydrothermal fluid flow on the bulk geochemical composition of the host rock. Samples from Nidd are dashed lines.

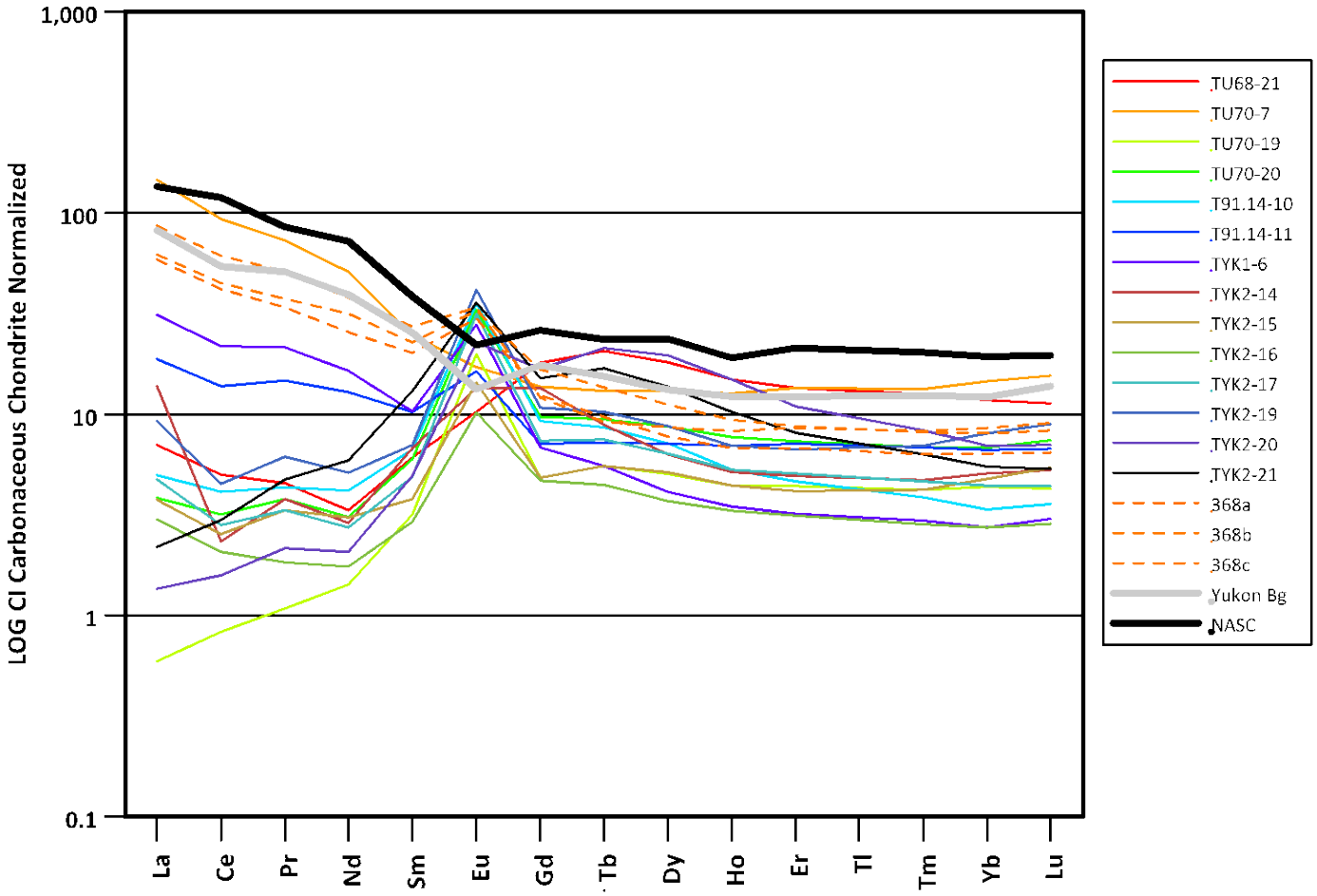

Figure 12. Rare earth element (REE) profile of vent samples from Tom (solid) and Nidd (dashed), compared to the Post-Archean Australian Shale (PAAS; McLennan, 1989). Data has been normalized to CI-Carbonaceous Chondritic composition (McDonough and Sun, 1995) and displayed on a log-normal plot.